POLITECNICO DI TORINO

Master's Degree in Aerospace Engineering

Master's Degree Thesis

Towards plasma-based swirling jets

Supervisors

Dr. Jacopo SERPIERI

Dr. Gioacchino CAFIERO

Paolo COMUNIAN

Candidate

Simone BUSELLI

292675

April 2024

Abstract

Adding an azimuthal velocity component to a stream coming out from a circular orifice leads to a swirling jet. Swirling jets are among the most common jet topologies present in industrial applications mostly thanks to their ability to enhance heat transfer [Huang, L. and El-Genk, M.S., 1998, in International Journal of Heat and Mass Transfer, 41.3, pp.583-600]. They are usually made by means of helicoidal insets installed in the nozzle outlet. Given their versatility of use and their low intrusiveness, plasma actuators (PAs) have been considered as flow control devices in jet flows; although, mainly for aeroacoustics purposes [Crawley, M., Kearney-Fischer, M. and Samimy, M., 2012, in 18th AIAA/CEAS Aeroacoustics Conference, p. 2211].

This preliminary study aimed to explore the feasibility of inducing a swirling motion to a circular jet by exploiting the momentum injection of the Dielectric barrier discharge plasma actuators (DBD-PAs).

Using high-resolution planar PIV, the wall jet produced by an array of DBD-PAs, in quiescent air, was investigated at various PAs input signal's voltage. The mechanical power output of the PAs was estimated from the time-averaged velocity fields obtained with PIV. This, together with electrical measurements assessing the consumed electrical power allowed estimating the efficiency at the tested operative conditions and for the considered configurations. Results indicate that with the current design only low swirl numbers could be obtained.

A comparison was made between actively and passively induced swirling jets. The latter were obtained by means of 3D-printed helical insets. Various swirl numbers were tested and the relative time-averaged velocity fields were retrieved using a five-hole probe. A plasma-based active swirler proof-of-concept was developed and tested. The obtained flow field was measured and compared against the unforced circular jet and the passively generated swirling jets.

The results obtained highlight a small and localized swirling effect underlining a control authority limited by the implemented design conditions.

Future developments should consider a measurement setup with an increased dynamic range and new PAs with greater authority.

Table of Contents

List of Tables

List of Figures

Acronyms

DBD
Dielectic Barrier Discarge

PA
Plasma Actuator

CRZ
Central Recirculation Zone

IR
Infrared Thermography

PIV
Particle Image Velocimetry

TKE
Turbulent Kinetic Energy

LAFPA
Localized Arc Filament Plasma Actuator

AC-DBD
Alternative Current Dielectric Barrier Discharge

NS-DBD
Nano-Second Dielectric Barrier Discarge

AFC
Active Flow Control

AoA

Angle of Attack

LDA

Laser Doppler Anemometry

PLA

Polylactic Acid

CCD

Charged-Coupled Device

CMOS

Complementary Metal Oxide Semiconductor

POD

Proper Orthogonal Decomposition

CAD

Computer-Aided Design

DoF

Degree of Freedom

DSA

Digital Sensor Array

HWA

Hot Wire Anemometry

Chapter 1

Declaration of intent

This presented study was aimed at exploring the suitability of plasma actuators as possible swirling generators in order to achieve a tunable, low intrusive, and switchable active device, able to overcome the limitations given by the fixed swirling passive insets usually used in technical applications such as in mixers, combustion chamber, and heat exchanger. Indeed, a new research topic with versatile applications for the flow control group of the Polytechnic University of Turin could be considered.
With the purpose of forcing a swirling effect to a circular free jet, the momentum injection of the Dielectric-Barrier-Discharge Plasma Actuators (DBD-PAs) has been exploited. In particular, the configuration chosen is formed by a short pipe with four wall-mounted streamwise oriented DBD-PAs equally spaced along the azimuthal direction (i.e. 90°).
Due to the lack of a structured benchmark of experimental campaigns concerning plasma actuators with this purpose a preliminary study was needed. Due to the exploring nature of this study, hand-made plasma actuators and 3D-printed components would be considered in order to limit the cost and the delivery time of commissioned parts. In particular, the thickness of the 3D printed pipe made of PLA would be exploited as a dielectric material that separates each couple of electrodes made through copper tape. Thanks to a layer of Kapton tape the external electrodes would be insulated to prevent the formation of unwanted plasma zones.
To extract information that can characterize the PAs made stand-alone and could be followed for future improvements in the design of this type of device, electrical and optical campaigns have been carried out. Different dielectric thicknesses and operating voltages have been tested.
Before moving to test the active swirling device designed in the jet facility some demonstrated passive swirling flow fields have been sampled in order to gain confidence and experience with the measurement technique available. Helical

passive insets with various empirical swirling numbers were printed and the inducted flow fields were measured with a pneumatic five-hole axial probe.
As the conclusion phase of this study, the designed plasma-based swirling device has been mounted and tested in the jet facility. A comparison between the forced and the unforced jet flow fields was made.

Chapter 2

Circular and swirling jets

2.1 Circular jets.

Jets are one of the most common features of fluid dynamics and one of the most studied ones. Various configurations and topologies of jets are present in different industrial applications especially to increase mixing or heat exchange properties. Due to their versatility of use, they have always been studied as a common topic of physics of fluid, moreover, they were studied to understand every feature of jet propulsion: the comprehension of their structures and turbulence characteristics and how to control them is the way through the mitigation of acoustic propagation and the optimization of thrust and mixing properties. The reference configuration of this fluid dynamic topic is the circular free jet which is used also as a reference flux for probe calibration.

Since they are not at all the newest topic of fluid dynamics, a lot of experimental data and theories are available in literature. To better frame the physics behind them, it will be reported below the classical model of the circular free jet. This flow field belongs to free shear flows such as wakes and mixing layers, all of them are characterized by the absence of walls or solid boundaries and by the presence of viscous effects. When a certain amount of mass flow comes out from a circular nozzle in a continuous way, the flow field develops with an axisymmetrical conical shape that spreads downstream due to the entrainment phenomenon. This flow field can be modeled in four different regions:

- Potential core: located very close to the nozzle, it presents a sort of top-hat velocity profile with the maximum velocity equal to the exit velocity from the orifice. For this reason, probe calibration processes take place in this region of the flow field.
- Mixing region: proceeding downstream, the front with the constant maximum

velocity begins to narrow, and the outer zones see a decreasing velocity due to the imposed matching with the external velocity which is zero.

- Transition region: the peak of velocity decreases with the distance from the nozzle.
- Self-similarity region: each velocity profile in this zone presents the same behavior, with an inflection point for each side where the maximum turbulence fluctuations are located. Profiles belonged to this region but at different axial positions can be overlapped if adequately dimensionless.

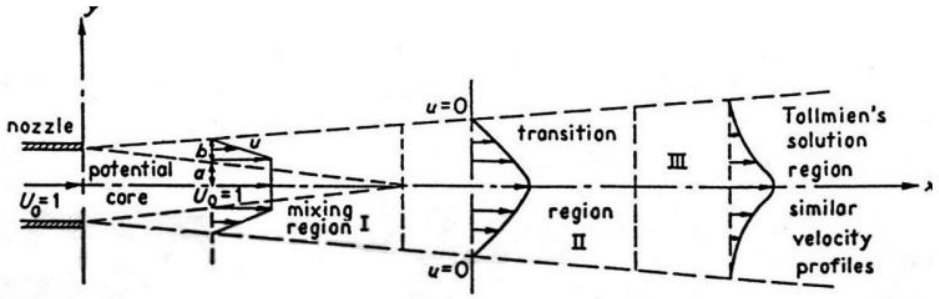

Figure 2.1: Circular free jet's regions.

2.2 Swirling jets

Adding a tangential or so-called swirl velocity to the stream coming out from the nozzle gives a whole different behavior at the flow field. These particular jets are called: Swirling jets. First of all, this additional velocity component causes the axial symmetry to be lost, with consequences in the selection of probes or techniques suitable for the measurement. These topology of jets are classified by a non-dimensional number called Swirl number which represents the ratio between the axial flux of tangential and axial momentum. Swirl number S is defined as follows [1]:

$$S = \frac{\int_0^{2\pi}\int_0^{\infty}\Big(\rho UW + \rho\langle u'w'\rangle\Big)r^2 dr d\theta}{\int_0^{2\pi}\int_0^{\infty}\Big(\rho U^2 + \rho\langle u'^2\rangle + (p-p_{\infty})\Big)r dr d\theta \cdot D/2}$$

where U and W are the mean velocities in axial and tangential directions, u' and w' their respectively fluctuations while ρ, p, D and r are: fluid density, static pressure, nozzle diameter and radial position. The above definition of swirl number is advantageous because both momentum fluxes are constant in free swirling jets

configuration so also S will be along the axial direction. [2]

There are two possible ways to give this additional velocity component: active and passive. The first one consists of spending energy to obtain the desired effects, for instance, counter-rotating pipes, additional tangential air injection, or moving parts are some possibilities. The passive ones are usually given by insets mounted on a nozzle that constrain the flow to follow a particular path, giving a helical behavior at the flow. Examples of configurations of swirling passive insets are shown in the figure below.

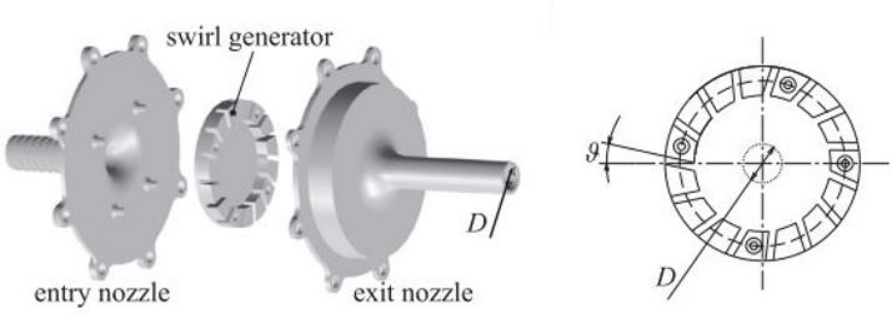

Figure 2.2: Schematic radial type swirler configuration. [3]

Figure 2.3: Sketch of an helicoidal inset. [4]

It is possible to operate a classification of jets through the previously defined swirl number S. A reasonable one is: non-swirling jets (S = 0), weakly swirling jets (0 < S < 0.6), strongly swirling jets before vortex breakdown (0.6 < S < 0.8) and strongly swirling jets with stable vortex breakdown with S > 0.8 [2]. It's important to specify that the aforementioned classification it's not universal and jets from the same S range can differ because jets are very sensitive to conditions upstream and to the way they are generated. For instance, the value of S where vortex breakdown occurs is not universal: Alekseenko et al [5] have observed the vortex breakdown to occur at S lower than 0.8.

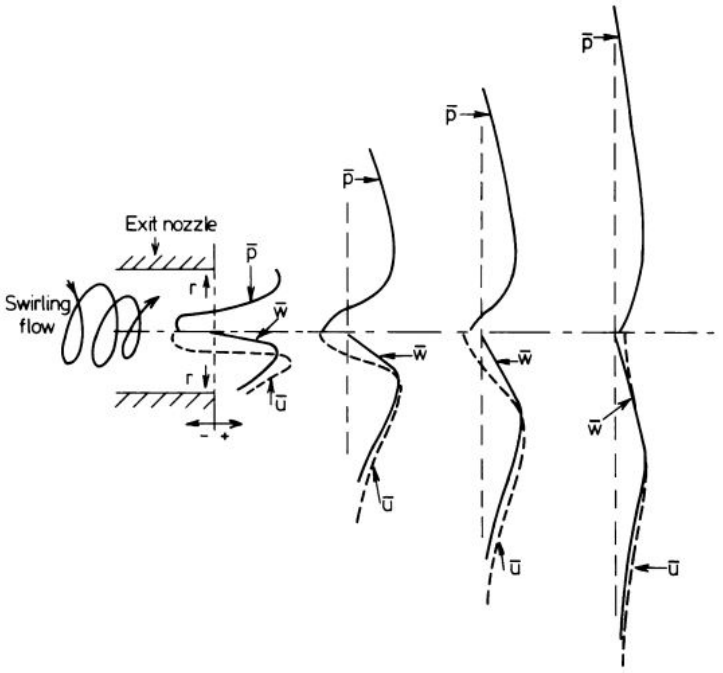

Figure 2.4: Schematic diagram of processing leading to CRZ formation.[1]

One of the most exploited behaviors of strongly swirling jets is the formation of a toroidal recirculation zone in the central jet's area. This recirculation zone (CRZ) takes place thanks to the radial pressure gradient naturally established by the tangential velocity component due to the centrifugal behavior of the stream and thanks also to the axial decay of the velocity component due to the expansion from the nozzle which generates a negative axial pressure gradient which causes this reverse flow and the formation of CRZ. Hence, this CRZ has been seen to be dependent on the decay of swirl velocity as swirling flow expands [6]. In a confined environment such as a combustion chamber, the swirling decay is reduced by the

presence of solid boundaries, affecting the CRZ formation in size and strength [7]. Combustion chambers are precisely one of the industrial applications of swirl jets as it has been seen how the formation of this CRZ could lead to flame stabilization.

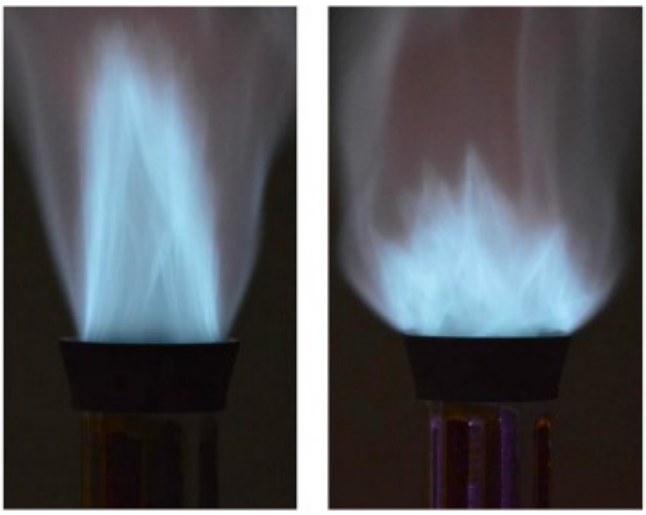

Figure 2.5: Visualization of flame with axial (left) and swirling (right) jet injector. [8]

2.3 Technical studies and application

In the following section some studies concerning swirling jets are reported. The first reported one made by Ianiro et al [4], compares the differences in terms of heat exchange properties between circular and swirling jets in an impinging configuration. In particular, the swirling motion was induced passively by multichannel helical inserts, and various Swirl numbers at fixed Reynolds numbers were investigated for different values of nozzle-to-plate distance with infrared thermography (IR) with the use of a heated thin foil sensor, in terms of Nusselt number (Nu) distribution. The Nusselt number is the dimensionless group that expresses the ratio between the heat exchanged through convection and the one exchanged through conduction and is expressed as;

$$Nu = \frac{hd}{\lambda}$$

where h is the convective coefficient, d is the reference length while λ is the thermal conductivity.
The authors highlight how heat transfer rate and uniformity are swirl number dependent but in particular show that: the multichannel jet without a helical path

induces a general enhancement in heat transfer compared to the circular impinging jet for lower nozzle-to-plate distances, while the swirl motion decreases the rate but increases the uniformity of heat transfer for nozzle-to-plate distances greater than six [4]. To assess the previous statements the authors compute and compare the averaged Nu on circular areas and the standard deviation percentage of Nu on the same circular areas for heat transfer rate and uniformity, respectively.

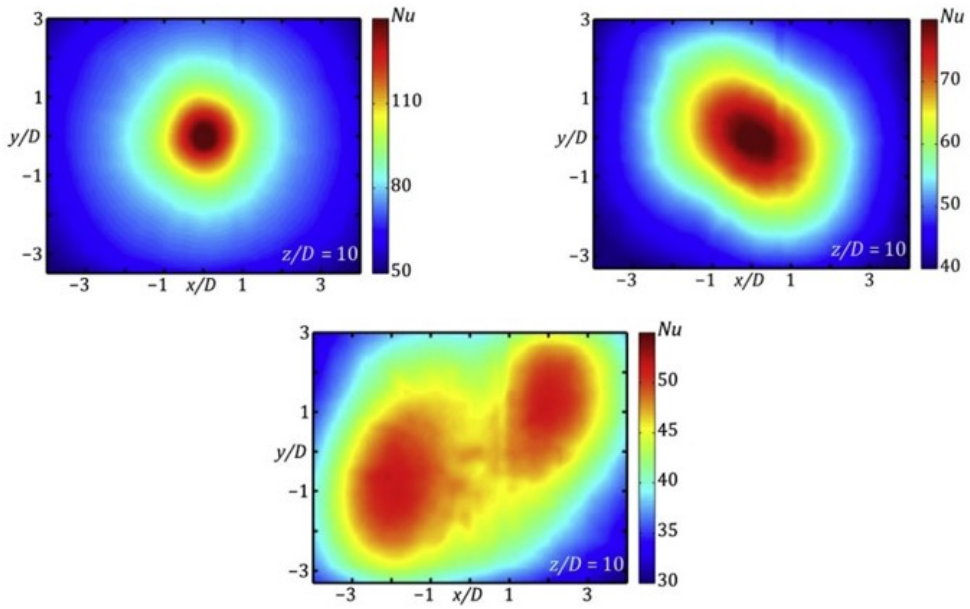

Figure 2.6: Nusselt distribution for circular (left), $S = 0$ (right), $S = 0.6$ (bottom) at nozzle-to-plate distance z/D = 10. [4]

Similar statements were already assessed by Huang L. and El-Genk M.S. [9] who observed an increased radial uniformity of heat exchange on the impinged surface for swirling jets in comparison with circular and multichannel ones. They noted an increased heat exchange for the multichannel (S=0) case (Figure 2.7), probably due to the restriction of the exit area.

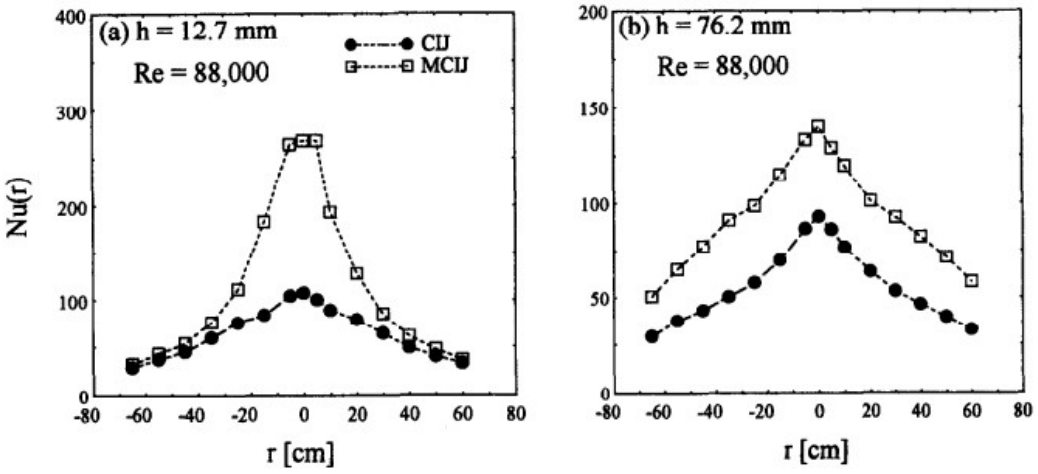

Figure 2.7: Comparison between Nu(r) values for multichannel S=0 (square) and circular (circle) impinging jets. [9]

Also the greater uniformity of heat exchange in the radial direction (Figure 2.8) was observed for different swirl angles (θ).

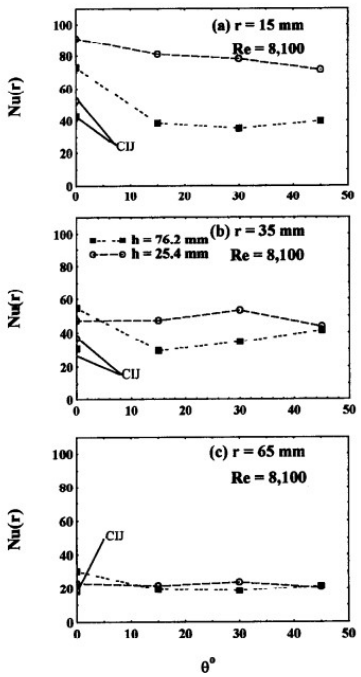

Figure 2.8: Effect of swirl angle on Nu(r) at a different radial position relative to the stagnation point. [9]

To better understand the flow structures differences between axial symmetric and swirling jets, that lead to the above-mentioned behavior in heat exchange and also for mixing purposes, PIV visualizations done by Aleeksenko et al [5] are reported. In Figure 2.9 the recirculation zone is visualized for an impinged swirling jet with Swirl number equal to 0.7.

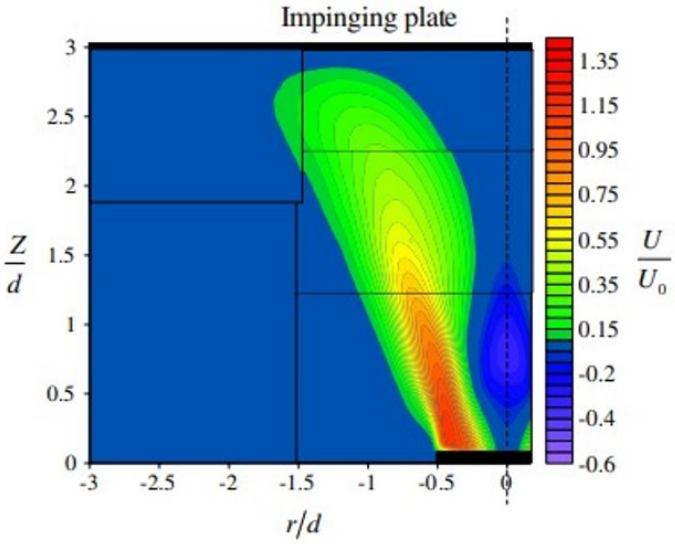

Figure 2.9: Distribution of the axial component of mean velocity normalized with the square of the exit mean velocity in the impinging jet with S=0.7 [5]

The authors map also the turbulent kinetic energy (TKE) for different swirl numbers (Figure 2.10). It can be noticed how for the low swirl rate, the distributions of the TKE components have high magnitudes in the area of the inner mixing layer, and they reach their maximum values close to the nozzle exit while, as expected, for greater swirl number, the maximum values of the TKE components are significantly higher than for lower swirl number. The local maxima of the radial component of the TKE are observed directly in the vicinity of the nozzle exit and in the region near z = 0.7d and r = 0.5d [5].

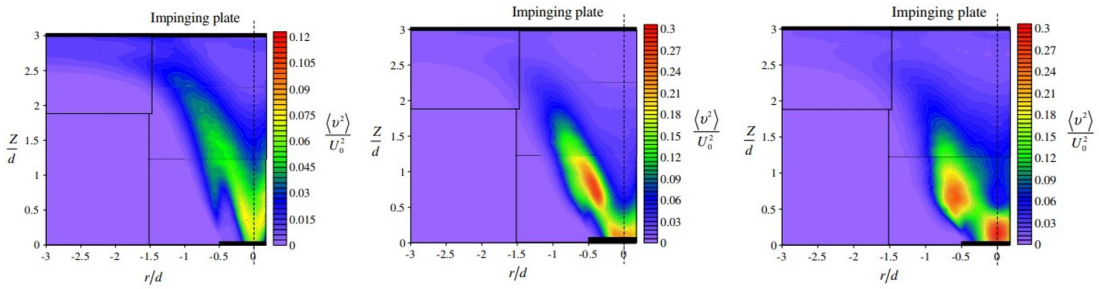

Figure 2.10: Distributions of the radial component of the turbulent kinetic energy normalized with the square of the exit mean velocity for different swirl number: S=0.41 (left), S=0.7 (center), S=1.0 (right)

Concluding this brief overview of experimental studies and visualizations it can be seen how for a circular jet, ring-like large-scale vortex structures develop in the jet's mixing layer according to the Kelvin–Helmholtz instability scenario and represent the result of several events of smaller vortex pairing, indeed, for a swirling jet case (S = 0.70), intense vortex spirals are observed and the breakdown of the flow symmetry directly from the origin takes place [5].

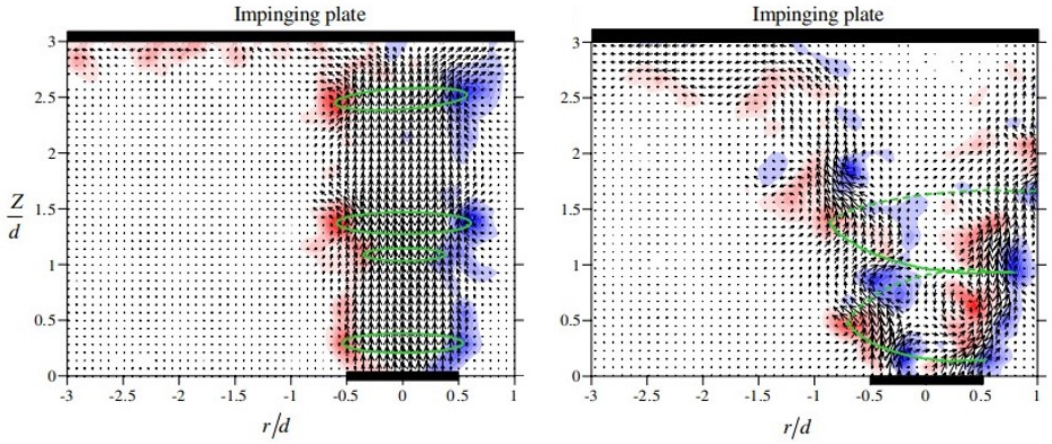

Figure 2.11: Instantaneous velocity and vorticity fields. Impinging jet at S = 0 (left) and S = 0.70 (right).

Chapter 3

Plasma actuators

The flow control studies aim to improve the aerodynamic characteristics of airfoils, to delay laminar to turbulent transition, or in general to optimize properties of certain flow fields. To do so, various techniques were invented and tested: active or passive ones which consist of spending energy or not to obtain these goals, respectively. Both types of techniques have their advantages and drawbacks depending on the problem in the exam. In general, the massive advantages that characterize active flow control techniques lie in the intensity of the actuation and in the possibility to switch on and off the effect as you wish. The first actuators on which research was carried out were hydraulic, acoustic, and mechanic, lately aeronautic scientific community has paid attention to particular actuators that exploit the generation of plasma-zones and plasma physics for flow control purposes. They have become of great interest especially for applications where moving parts of mechanical actuators should be avoided, or for flow control applications requiring a fast time response as well as for their ability to generate jets that are very attached and parallel to the wall. For instance, due to that characteristic, they're a serious candidate for boundary layer flow control future techniques and consequently for drag reduction studies.

Plasma is an ionized fluid consisting of a collection of charged particles but is electrically neutral overall. It is also known as the fourth state of matter. Some of the most spectacular atmospheric events such as northern lights and thunderbolts involve plasma formation. The process of the plasma formation is achieved by applying a voltage at a certain level, known as "breakdown voltage", to fluid such as a gas mixture, which saturates and changes its electrical properties moving from an insulating behavior to a conductive one. In this process, the gas begins to generate random discharges which, by increasing the voltages, can lead to the formation of an electrical arc which, once established, requires a lower voltage to be maintained. An example of the voltage-current trend in a plasma formation process is illustrated in the figure below.

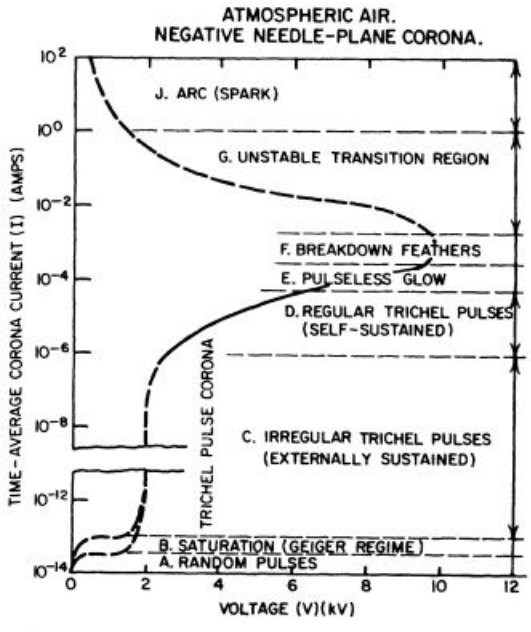

Figure 3.1: Schematic voltage - current trend for air around atmospheric pressure. [10]

3.1 PAs types and operating principles

A typical configuration of plasma actuators (PAs) requires the presence of a dielectric layer between two geometrically staggered electrodes, typically long and thin, integrated into an aerodynamic surface, to which a high electric field is applied bringing the gas to saturation, causes the plasma to be formed and the discharges to occur.
As a result of plasma zone formation, the main effects exploited for aerodynamic purpose are:

- Momentum transfer due to the collisions of charged particles, accelerated by the Lorentz and/or Coulomb forces, to the neutral surrounded gas.
- Thermal heating by Joule effect.

To better frame the physical effects of plasma zone formation in the aerodynamic context it is important to highlight how the discharge processes that take place in the plasma zone are from four to eight orders of magnitude, both spatially and temporally, lower than those of aerodynamic interest, therefore the aforementioned effect that PAs give to the flow field can be seen as quasi-steady state. [11].

Some examples of plasma-based flow control actuators are the alternating current dielectric barrier discharge (AC-DBD) which are based on the momentum transfer effects given by the establishment of the electromagnetic interaction inside the plasma region. Instead, some PAs based on fast thermal heating are localized arc filament actuators (LAFPA) and nanosecond dielectric barrier discharge (NS-DBD). Both of them exploit the compression waves generated by the local fast thermal heating produced by the high current pulsed electrical discharges, which, for instance, can excite also supersonic jets' instabilities. The main difference between these two classes of PAs consists in the perturbations that they can give to the flow field, for instance, LAFPAs are the ones that confer perturbations with greater amplitude and bandwidth. Due to that, they are suitable for high-speed and high-turbulence applications. To better frame the range of applications of every class of PAs it is important to underline how as the Reynolds number (Re) grows, so do the frequency bands of the Kelvin-Helmotz instabilities as well as the amplitude of perturbations needed to excite them [12]. Kelvin-Helmotz linear instability is essentially an inviscid instability that governs the starting phase of the perturbation growth, therefore acting on these instabilities can give a sort of control over the turbulence dynamics of various flows. These perturbations don't act the same for each frequency but have usually two preferred frequency bands. To identify these two frequencies for various flows without losing universally, they can be dimensionless giving birth to a dimensionless number known as Strouhal number $St = \frac{fL}{U}$, where f is the frequency, L is a reference length and U a reference speed. Depending on the reference length chosen, two characteristic frequencies are identified: the first one is given by the choice of the momentum thickness as length, while the second is given by a characteristic length of the geometry like the diameter or chord of an airfoil. Obviously, following the scale of the reference length order, these two frequencies of perturbation don't act the same on the turbulence dynamics: the one related to momentum thickness acts on the development of the smallest turbulence structures while the other promotes the development of large coherent turbulent structures [13].
At the expense of the different physical principles exploited, at the geometry level, both NS-DBD and AC-DBD stand with the configuration mentioned at the beginning with superficial electrodes but the main difference that causes the diversity in actuation stands in the waveform of the input tension signal (order of magnitude about 10 kV) which is a pulsed wave for NS-DBD (order of 50 ns) while for AC-DBD is a sinusoidal signal.

For all these reasons NS-DBDs and LAFPAs are suitable for high-speed flows with the first ones more suitable for spatially distributed actuation such as AFC over airfoils while AC-DBD PAs range of operation is limited to low subsonic flows. For instance, some studies on separation control over airfoils underline how AC-DBDs

control authority seems to be limited to free stream velocity of order about 50 ms^{-1} [14] till an asymptotic limit around 135 ms^{-1} [15] increasing input voltage and dielectric thickness.

3.2 Technical applications and studies

Plasma-based actuators are a very young technology that started to captivate the aeronautical community in the mid-1990s and at the moment are far from an industrial application mainly due to lack of testing under various environmental operating conditions, complexity in integration mostly due to electromagnetic compatibility with other system, and the miniaturization problem of the power supply needed. At the end of this brief PAs overview, it will be reported some experimental relevant AFC studies such as attachment and detachment of flows, turbulence transition delay, and noise reduction.

N.Benard et al [16] have led a study involving DBD-PAs about the forced detachment and re-attachment of flow in a diffuser mounted at the exit of an axisymmetric jet with the aim to investigate the future feasibility of DBD-PAs as jet vectoring actuators. The two configurations are illustrated in Figure 3.2. This study highlights

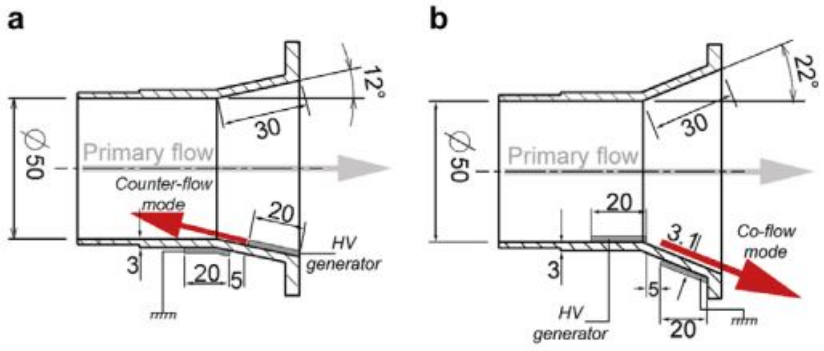

Figure 3.2: Diffuser configurations for forced detachment (a) and re-attachment (b) of flow [16].

how the single DBD-PA acting is limited to a forced re-attachment of a jet with an exit velocity around 20 ms^{-1} while the detachment can be forced to jet with an exit velocity till 30 ms^{-1}. Other relevant information assessed in this study is how easier is the forced detachment of a flow with respect to an attachment of a naturally detached flow, also due to the time of actuation requested. Another important application of DBD-PAs, always dealing with flow separation control, concerns the re-attachment of flow to delay the separation at high angles of attack. For

instance, Akansu et al [17] carried out an experimental study with four DBD-PAs placed at various chord positions over a NACA0015 airfoil at Reynolds number equal to 15000. Their results highlight how activating a different combination of their actuators, they were able to reattach the naturally separated flow up to 15° angles of attack (AoA) with a peak-to-peak voltage of 12 kV while in order to have the control authority to reattach the flow for 20° AoA they needed to increase the input voltage to 13 kV but taking care to double the dielectric thickness to avoid the generation of unwanted arc.

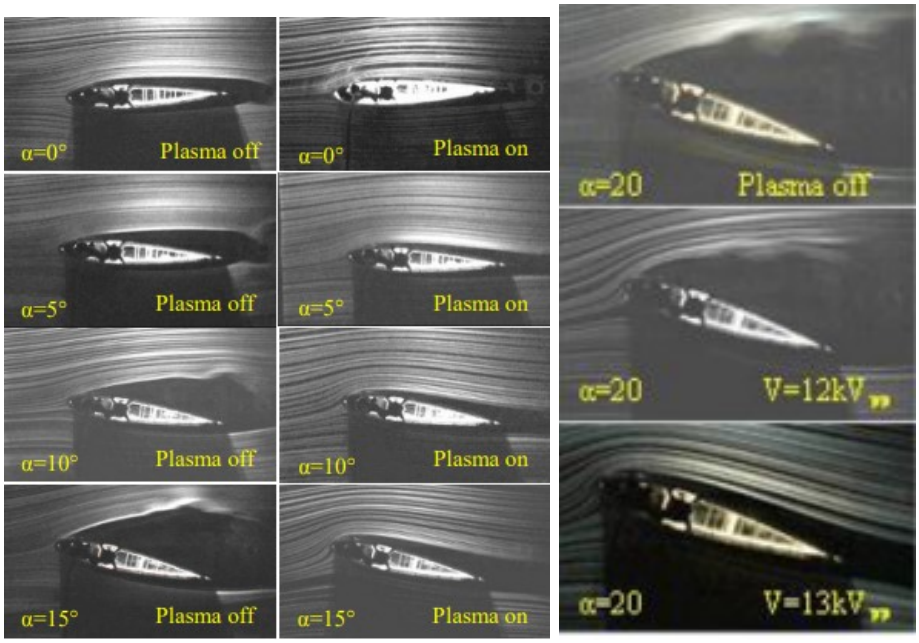

Figure 3.3: Visualization of forced re-attachment of flow over NACA0015 airfoil thanks to DBD-PAs [17]

Other relevant work that underlines the wide range of applications that plasma actuators may have in future, concerns the use of DBD-PAs in steady and pulsed actuation with the aim to delay the transition over a flat plate, more specifically Grundmann and Tropea [18] tried to cancel artificially excited Tollmien–Schlichting waves over a flat plate. The body force induced by the actuators in the boundary layer attenuates the aforementioned waves changing the velocity profiles. Through Laser Doppler Anemometry (LDA) they were able to capture the velocity profiles inside the boundary layer and estimate the shape factors (H_{12}) at various downstream positions, i.e. the ratio between the displacement thickness (δ_1) and the momentum thickness (δ_2) which definitions are below listed.

$$\delta_1 = \int_0^\infty \left(1 - \frac{U}{U_\infty}\right) dy$$

$$\delta_2 = \int_0^\infty \frac{U}{U_\infty}\left(1 - \frac{U}{U_\infty}\right)dy$$

Referring to a Blasius boundary-layer, which is a laminar one with a null pressure gradient, shape factor is equal to 2.59. An adverse pressure gradient tends to increase the value of the shape factor, while a favorable one tends to decrease it to a minimum value of about 2. Lower values of the shape factor indicate turbulent profiles. From the value sampled and computed in these experiments plasma actuators delayed the transition by approximately 200 mm [18].

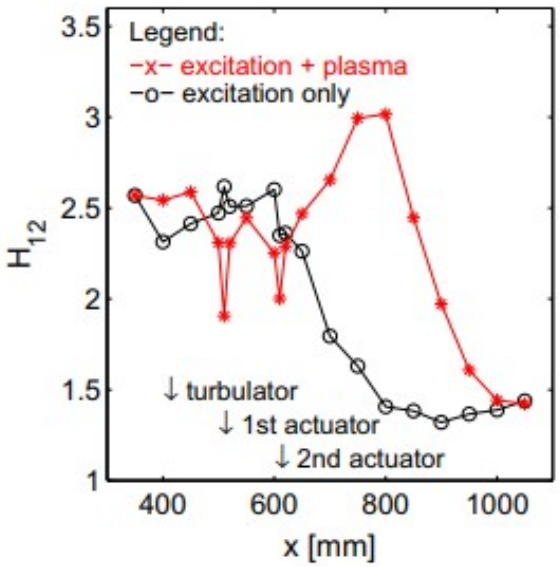

Figure 3.4: Shape factor with and without plasma control over a flat plate. [18]

While the studies presented so far concern non-thermal plasma actuators,i.e. DBD-PAs, to complete this brief overview it will be now presented some studies concerning thermal actuators, in particular concerning the LAFPA configuration. As before mentioned, these actuators have a greater amplitude in excitation leading them to be suitable also for flow control purposes of high Reynolds and high-speed flows, therefore the following studies will concern also supersonic flows instead of the previously presented subsonic ones. The first study reported concerns the control authority of a supersonic axisymmetric jet employing eight LAFPAs equally phased around the circular nozzle. It was carried out by Kim and Samimy [19]. They forced a supersonic jet in over-expanded, perfectly, and under-expanded conditions, respectively Mach numbers equal to 1.2, 1.3, and 1.4 with Reynold numbers ranging from $1.2 \cdot 10^6$ to $1.4 \cdot 10^6$ forcing at various Strouhal numbers covering the range between the Strouhal number of the shear layer instability and the jet column one, the one defined with the displacement thickness and geometrical length, respectively.

Comparing the forced case with the baseline, i.e unforced, they assessed that only some forcing Strouhal numbers are effective in manipulating jet instabilities and indeed spreading and mixing properties, in particular for the M=1.3 they found an optimal forcing Strouhal number in terms of enhancing the spreading rate and a threshold value, which if exceeded it doesn't affect the spreading rate of the jet.

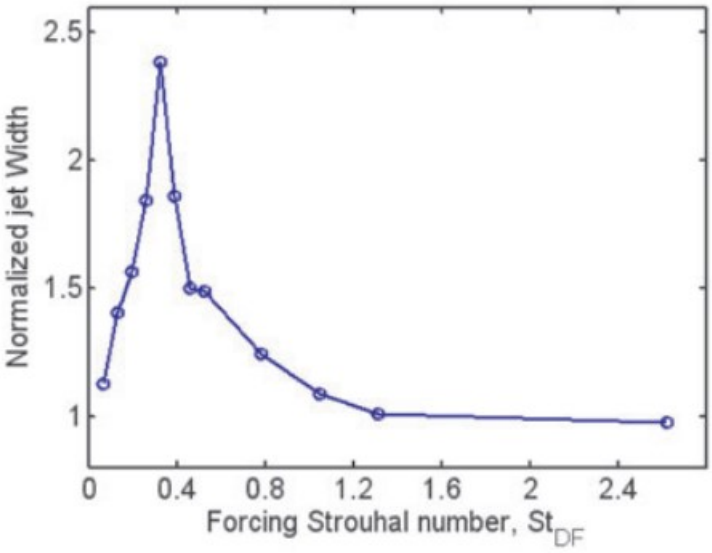

Figure 3.5: Normalized jet widths (with the baseline one) at x/D = 10 for the same azimuthal mode at various forcing St number. [19]

In the over-expanded (M = 1.2) and under-expanded (M = 1.4) jets, Kim and Samimy noticed the generation of structures with a reduced strength compared to those in the perfectly-expanded jet. According to the authors, the reduced strength of the vortical structures is believed to be due to the competition for energy and growth between naturally amplified, due to the flow-acoustic feedback loop, and forced structures [19].

With the same thermal PAs configuration also studies over non-axisymmetric jet were carried out, in particular, is below reported the study done by M. Crawley, M. Kearney-Fischer and M. Samimy [20] about an ideally expanded, unheated Mach 1.5 rectangular jet with an aspect ratio of 2, Reynolds number of $\sim 1.5 \cdot 10^6$ forced using till eight operating LAFPAs, for noise control purpose. During this study, five different modes were investigated varying the actuators which were operating at the same time with forcing Strouhal numbers ranging from 0.1 to 4.0. They found that for all the recorded tests there was a reduction in the far field

noise at low polar angles (i.e. angle spanned in the plane formed by the jet axis and the minor axis of the rectangular section) and how this reduction is forcing Strouhal number dependent. The most effective mode between the explored one is the center-diagonal (CD) composed of the four actuators located in the middle of the edge for phase 0 and the four external ones located along the major axis (of the total six) for phase π. In particular, they obtained a maximum reduction of roughly 2 dB in the downstream direction for a Strouhal number equal to 0.8. [20]

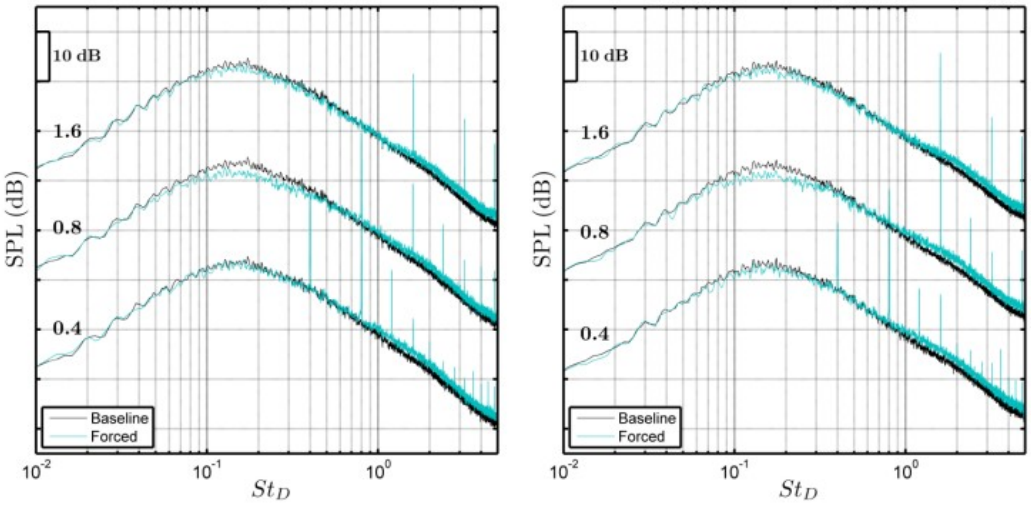

Figure 3.6: Acoustic spectra for CD forcing mode, $St_F = 0.4$, 0.8, and 1.6, for $= 30°$, in major axis direction (left) and minor axis one (right) [20]

Chapter 4

Toward plasma induced swirl jets

As mentioned in Chapter 1 the idea behind this project is to induce a tangential velocity through DBD-PAs placed streamwise along the axial coordinate of a PLA 3D printed short pipe inset. After some qualitative visualization over PLA sheets, the solution with a thin kapton layer over a PLA wall has been discarded due to a not-so-visible, and indeed effective, plasma zone detection at available operating voltage. So, our configuration involves only the PLA wall as a dielectric barrier that separates the two thin copper electrodes. For the experimental activities that will be presented in the following sections the test sample is composed by a section of a short pipe (cut along the axial direction), $L = 6.7\ cm$ long, made of PLA with an inner diameter of $D_{in} = 25.4\ mm$ and a variable thickness ($t_{diel} = 1\ mm$, $t_{diel} = 1.25\ mm$) with three hand-made DBD-PAs each one presenting a couple of copper electrodes, one insulated by kapton tape outside and one exposed to the air placed in the inner part of the virtual cylinder so that only in the inner part of the cylinder plasma zones will be formed (Figure 4.1). The dimensions of electrodes (Table 4.1) comport a plasma length of about $L_p = 4\ cm$.

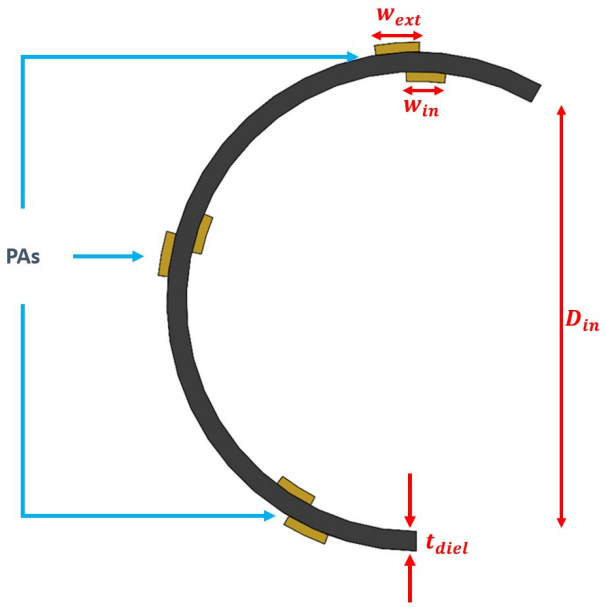

Figure 4.1: Sketch of the sample.

	$t_{diel} = 1\ mm$	$t_{diel} = 1.25mm$
$w_{in}\ [mm]$	3	3
$w_{ext}\ [mm]$	5	5
$L_{in}\ [mm]$	50	50
$L_{ext}\ [mm]$	57	57

Table 4.1: Sizing of the electrodes with reference to Figure 4.1.

4.1 Electrical characterization.

The sizing of a power supplier for possible future industrialization as long as the electrical efficiency or impedance matching are not the main purposes of this work. However, a small electrical characterization campaign was carried out to estimate the power consumption and to compute a sort of effectiveness after some fluid dynamics measurements. There are two methods to estimate power consumption: one involves recording the current signal through a probe resistor while the second is the so-called monitor capacitor method, which presents a probe capacitor placed between the PAs and the ground. The most simple and convenient method [18], used in this study, is the latter due to the fact that current behavior would present a lot of spikes, indicating a lower signal-to-noise ratio, that would need to be filtered while using a capacitor, the self-filtering properties of capacitors given by the

capacitor concept can be exploited, since it integrates the current passing through the actuator in time and thus captures all occurring micro-discharge pulses, leading to a better signal to noise ratio [21]. The right capacitance needs to be chosen: in fact, following the equation of an equivalent capacitance for parallel capacitors, an excessively low capacitance would alter the circuit properties falsifying the power consumption estimation while a too-high one would result in a signal with a high signal-to-noise ratio that would need to be filtered further ($C_P \propto \frac{1}{V_P}$).

$$\frac{1}{C_{tot}} = \frac{1}{C_a} + \frac{1}{C_P} \implies C_{tot} \simeq C_a$$

Indeed for $C_P >> C_a$ the total capacitance of the circuit will be unaltered. A sketch of the electrical circuit for a case with a single DBD-PA is shown in Figure 4.2.

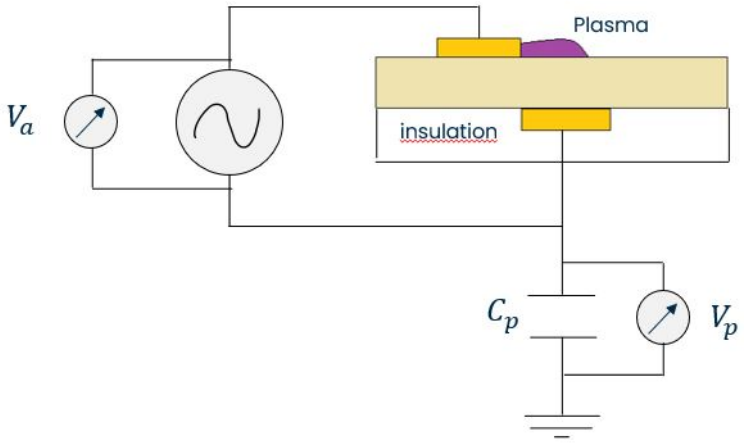

Figure 4.2: Sketch of the electrical circuit for a case with a single DBD-PA.

Once recorded the voltage signal of the capacitor it is needed to do some steps to obtain the power consumption estimation. Indeed, it can be assessed that the charge stored Q_P by the capacitor is proportional to the voltage signal through the value of the capacitance (constant in this case),

$$Q_P(t) = C_P V_P(t)$$

plotting the charge stored against the voltage signal V_P will result in a Q-V cyclogram (Figure 4.3), known as Lissajous curve, for each cycle. Due to the fact

that the current passing through the capacitor is the same as the one passing through the PA (C_P doesn't affect the circuit total capacitance) and that V_P is negligible with respect of PA's voltage V_a, exploiting the definition of capacitance

$$C = \frac{dQ}{dV}$$

and current ($I(t) = \frac{dV(t)}{dt}$) it can be stated that the area enclosed by this curve is the energy consumed per cycle, integrating along the time, consumption estimation P_a will be obtained [21].

$$P_a(t) = V_a(t)I_a(t) = V_a(t)C_P\frac{dV_P}{dt}$$

$$\overline{P_a} = \frac{1}{T}\int_0^T P_a(t) = \frac{1}{T}\int V_a C_P dV_P = \frac{1}{T}\oint V_a dQ_P$$

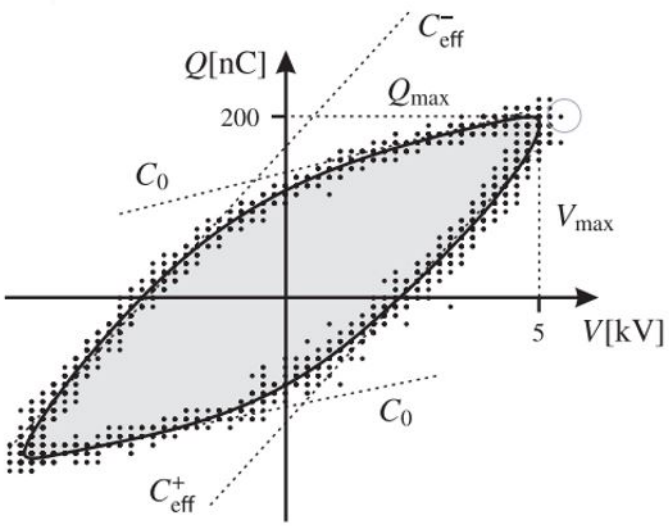

Figure 4.3: Lissajous curve with raw and filtered data [21].

As indicated in Figure 4.3 taken from [21] they can be identified two couples of tangents which their respectively slopes represent the two different capacitance: C_{eff} and C_0. The latter one is a sort of "cold capacitance" or rather the material capacitance property of PA when is turned off, while the first one is the capacitance of the actuator when turned on. Roughly C_{eff} can be seen as composed of two serial capacitors: one with C_0 and one due to the gas that had been ionized C_{gas}.

Despite all the consideration regarding the signal to noise ratio, it's important to underline how further post-processing and filtering are needed to extract some numerical robust information. The following results are obtained in accord with the above-mentioned equations after having filtered and smoothed the voltage signals with a Savitzky-Golay filter [22], based on a local least squares polynomial smoothing.

4.1.1 Experimental set up.

The experimental setup (Figure 4.4) used for these electrical investigations comprehends: a power supply (Voltcraft VSP-2410), a function generator (Thandar TG2001), and a digital oscilloscope (NI VB-8012) as illustrated in Figure 4.5, a series of ceramic capacitors with different capacitances with a probe able to scale the voltage capacitor recording by an attenuation factor x10, and the high voltage - high frequency kit GBS Elektronik GmbH Minipuls 4 (Figure 4.6). The latter comprehends a transformer cascade able to generate AC voltage up to 20 kV peak and a bridge converter that delivers a powerful low voltage square wave which the cascade transforms up and filters out a sine-like waveform.

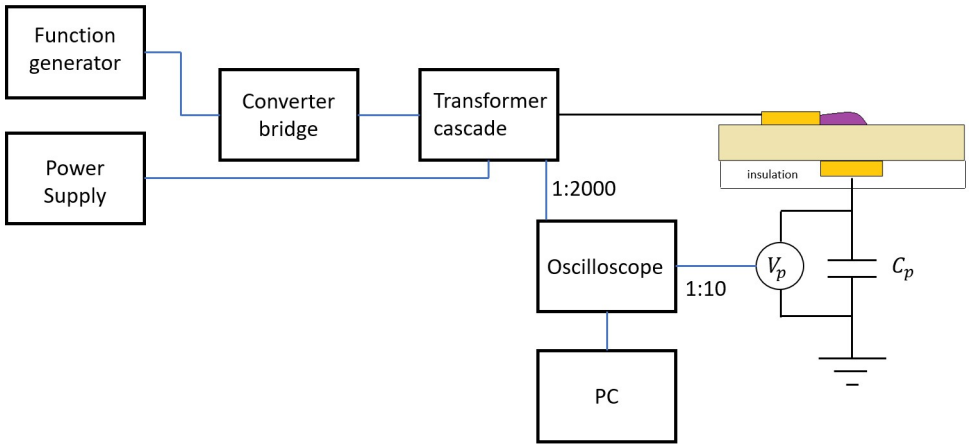

Figure 4.4: Sketch of the experimental set up

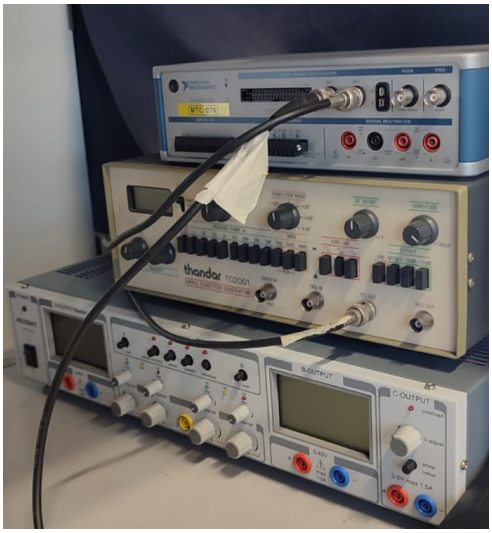

Figure 4.5: From top to bottom: oscilloscope, function generator and power supply.

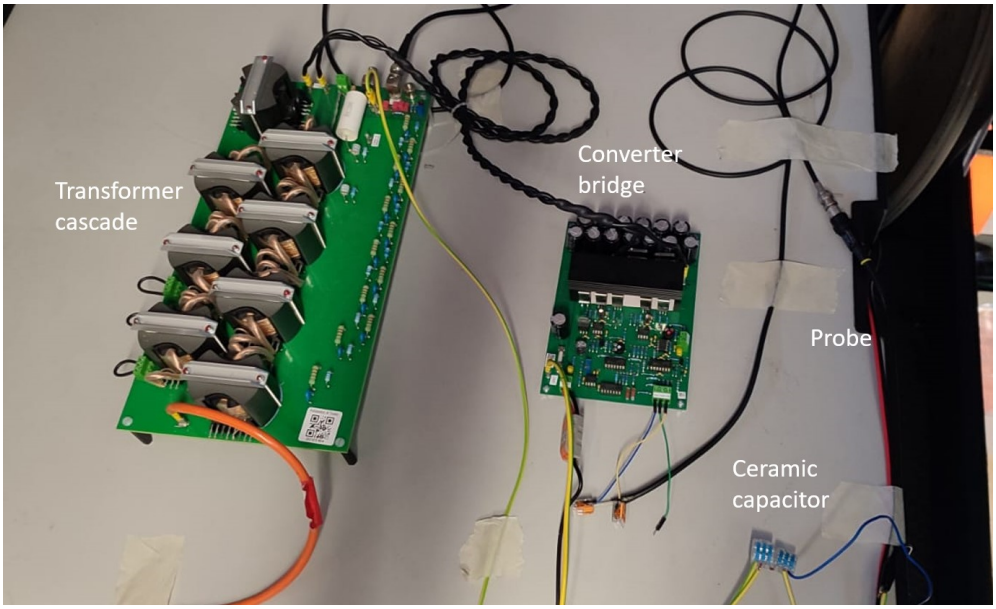

Figure 4.6: High voltage - high frequency system.

4.1.2 Results

The first evaluation carried out for the electrical characterization was aimed at choosing the correct capacitor. To check his independence in the circuit several capacitances were tested in a single operative condition, evaluating the mean area

enclosed by the cyclograms described, multiplied by frequency and the respective capacitance, and plotting against the latter. The operating conditions were the following:

- Dielectric thickness: $t = 1.25\ mm$
- Operating voltage: $V_{pp} = 10\ kV$
- Operating frequency: $f = 12\ kHz$
- Plasma length: $L = 4.5\ mm$ (x 3 DBD-PAs)
- Sampling frequency: $f_s = 10\ MHz$
- Sampling period: $T_s = 0.05\ s$

C_p	75 pF	150 pF	220 pF	253 pF	330 pF	470 pF	1 nF	1.5 nF

Table 4.2: Probe capacitance test matrix.

The mean area $\overline{A_s}$ enclosed by each test case are reported in Figure 4.7. Each plotted point is the average over roughly 600 cycles, each described by about 800 points.

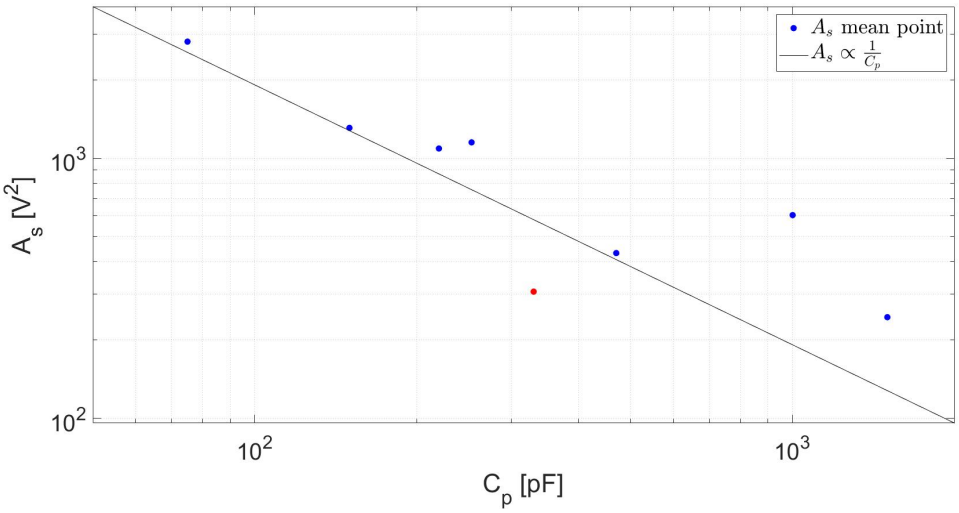

Figure 4.7: Mean area enclosed by each cyclograms plotted against probe capacitance.

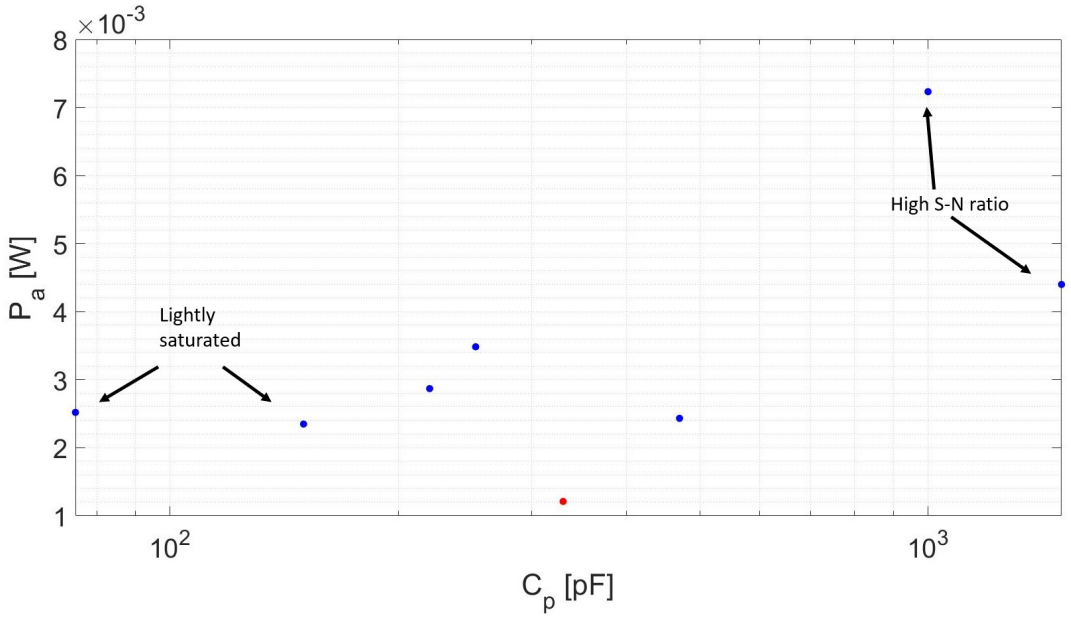

Figure 4.8: Mean power consumption plotted against probe capacitance.

From these values it was possible to plot the mean power consumption values (Figure 4.8) for the operative condition chosen. As reported the first two probe capacitances present a light saturation (Figure 4.9) while the last two of the test matrix (Table 4.2) present signals with a high signal-to-noise ratio (Figure 4.10)

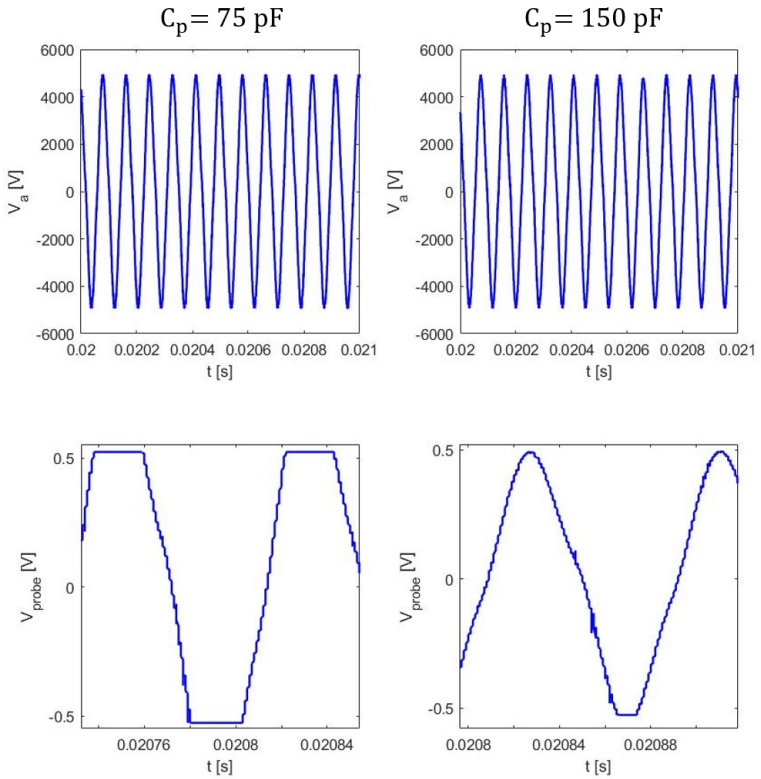

Figure 4.9: Recorded voltage signals for $C_p = 75,\ 150\ nF$

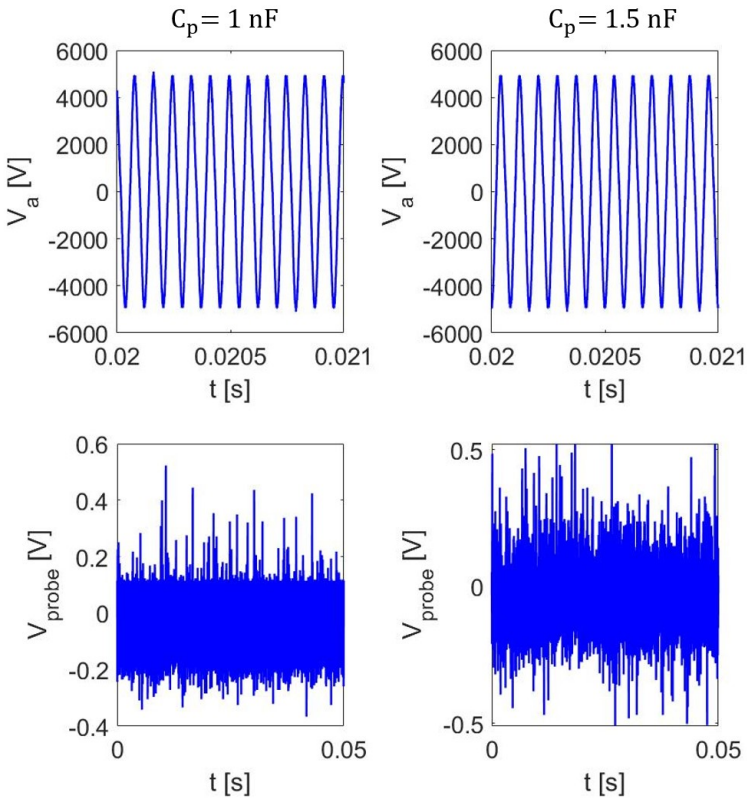

Figure 4.10: Recorded voltage signals for $C_p = 1,\ 1.5\ nF$

C_p	A_s $[V^2]$	σ_{A_s} $[V^2]$	P_a [W]	σ_{P_a} [W]
75 pF	2808.6	56.8406	$2.5 \cdot 10^{-3}$	$0.0510 \cdot 10^{-3}$
150 pF	1310.0	46.8663	$2.4 \cdot 10^{-3}$	$0.0841 \cdot 10^{-3}$
220 pF	1093.0	28.7107	$2.9 \cdot 10^{-3}$	$0.0755 \cdot 10^{-3}$
253 pF	1153.0	31.8384	$3.5 \cdot 10^{-3}$	$0.0963 \cdot 10^{-3}$
330 pF	317.0	79.3788	$1.3 \cdot 10^{-3}$	$0.3133 \cdot 10^{-3}$
470 pF	437.1	18.3573	$2.5 \cdot 10^{-3}$	$0.1034 \cdot 10^{-3}$
1 nF	608.0	36.2837	$7.3 \cdot 10^{-3}$	$0.4295 \cdot 10^{-3}$
1.5 nF	279.0	16.4061	$5.0 \cdot 10^{-3}$	$0.2948 \cdot 10^{-3}$

Table 4.3: Result Matrix for each C_p tested.

As it can be seen, the A_s enclosed by the cyclograms recorded with a capacitor with $C_p = 330\ pF$ have a too high standard deviation (about 25%), so that measures have to be discarded. After these considerations and analyzing also the smoothness of the signals recorded it was chosen a ceramic probe capacitor of 220 pF.

After the choice of the capacitor, it was possible to estimate the electrical power consumption for different operating conditions that in the following section we are going to characterize also mechanically. For this preliminary study, only two different dielectric thicknesses $t = 1\ mm$ and $t = 1.25\ mm$ were tested. Unfortunately, thinner PLA walls, therefore thinner dielectric barriers, were not so homogeneous due to 3D filament printing limits that comport a bad dielectric behavior and durability for plasma generation, and, for instance, $t = 0.8\ mm$ test case was discarded after some electrical tests. At the same time, a thicker PLA wall would have had lower capacitance, for instance, the capacitance of an ideal infinite plain capacitor scales with the inverse of the dielectric thickness (the gap between the plates) $C \propto \frac{1}{t}$, hence the effect of plasma generation would have been minor. Furthermore, a thick full-filled wall is the opposite of the filament 3D printing purpose and philosophy and would have also comported a longer printing times and promptness. As operating conditions, they were tested three operating voltages 10 kV, 11 kV, 12 kV at fixed operating frequency 12 kHz while sampling frequency and sampling period were the same of the probe capacitance sizing tests. The results are reported in Table 4.4, while examples of the cyclograms obtained are presented in Figure 4.11-4.13. As predictable, power consumption seems to increase with increasing operating voltage and with the thinner dielectric thickness case, hopefully, due to more effective and strong plasma zones.

V_{pp} [kV]	$\overline{P_a} \pm \sigma_{P_a}$ [W] $t = 1\ mm$	$\overline{P_a} \pm \sigma_{P_a}$ [W] $t = 1.25\ mm$
10	$(6.2 \pm 0.1807) \cdot 10^{-3}$	$(3.5 \pm 0.1001) \cdot 10^{-3}$
11	$(8.0 \pm 0.1680) \cdot 10^{-3}$	$(4.9 \pm 0.1364) \cdot 10^{-3}$
12	$(10.4 \pm 0.2346) \cdot 10^{-3}$	$(6.7 \pm 0.1313) \cdot 10^{-3}$

Table 4.4: Electrical characterization three 3 DBD-PAs in three different operating conditions: mean and standard deviation values.

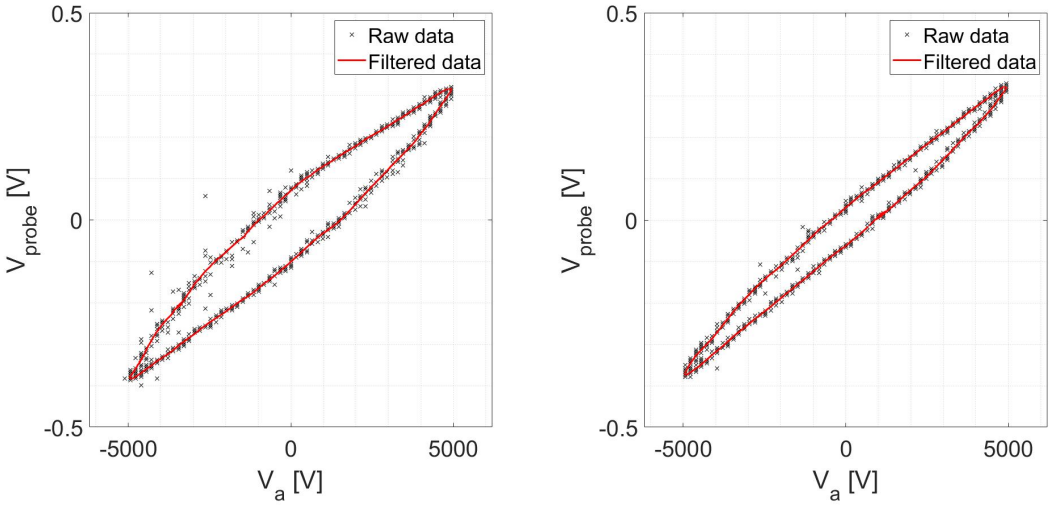

$t = 1\ mm.$ $t = 1.25\ mm.$

Figure 4.11: Examples of a cyclogram with raw and filtered data for the two dielectric thicknesses t tested at $V_{pp} = 10\ kV$ and $f = 12\ kHz$.

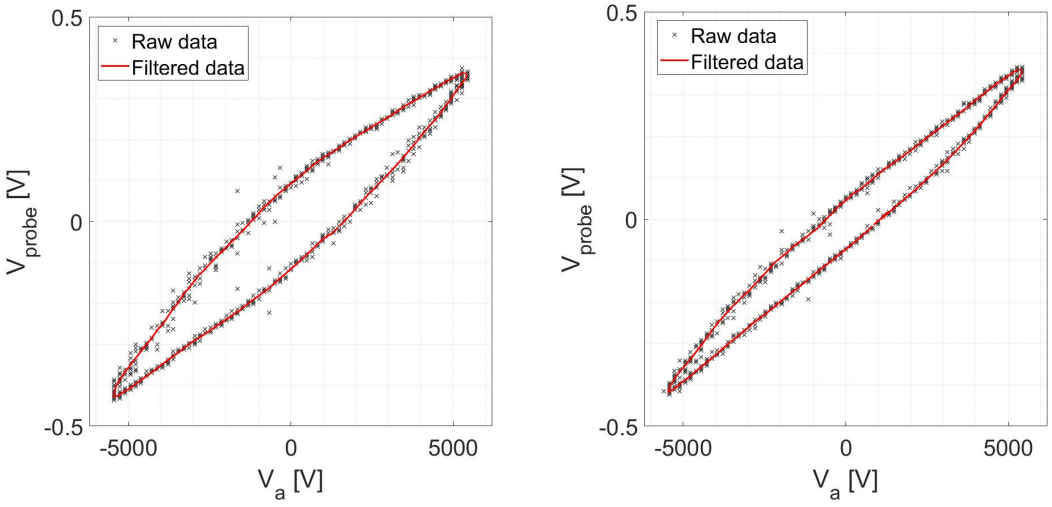

$t = 1\ mm.$ $t = 1.25\ mm.$

Figure 4.12: Examples of a cyclogram with raw and filtered data for the two dielectric thicknesses tested at $V_{pp} = 11\ kV$ and $f = 12\ kHz$.

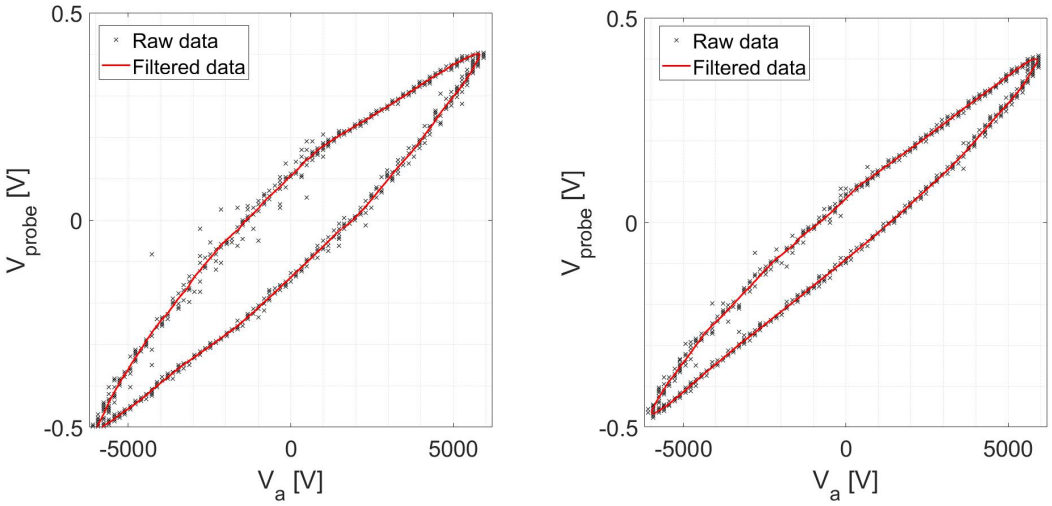

$t = 1\ mm.$ $t = 1.25\ mm.$

Figure 4.13: Examples of a cyclogram with raw and filtered data for the two dielectric thicknesses tested at $V_{pp} = 12\ kV$ and $f = 12\ kHz$.

4.2 PIV campaign.

4.2.1 PIV overview.

Particle Image Velocimetry (PIV) is an optical non-intrusive technique that guarantees a high space resolution instantaneous velocity field thanks to its high-density velocity vector field detection, while the time resolution is not on the same order of magnitude, in fact at the beginning of the PIV development the frame rate was at the order of few Hz, but over time the low time resolution was partially overcome, increasing it up to a thousand Hz in the PIV time-resolved configuration. Various "geometrical" configurations of this technique differ in the number of velocity components that can be detected. The canon form, and the one implemented in the following campaign, is the planar PIV that can capture the velocity vectors with two components in a plane (2D). To add the third component coming out from the recording plane it is needed almost a second camera, indeed this topology can detect all velocity components but only in a bi-dimensional space, and it's known as Stereo PIV. Therefore to capture velocity vectors in an instantaneous volume (three-dimensional space) are needed more cameras, usually almost four; this topology is called Tomographic PIV. More in detail, a PIV setup needs a laser source able to emit a coherent and mono-chromatic laser ray and a set of lenses able to open up the ray in order to form a very thin plane of laser light. This laser

plane enlightens the measurement plane and in particular small particles that have been previously and appropriately seeded in the flow field. A CCD or better CMOS camera has to record perpendicularly this illuminated seeded plane. The way the camera records and therefore the laser is emitted affects the time resolution: if the laser source emits pulses intermittently the time resolution would be low as the camera must take snapshots at the same moments as the field is illuminated. The simultaneous between the camera taking snapshots and the laser source emitting is given by the presence of a synchronizer system. Instead, if the laser source can emit and the high-resolution camera to record continuously the time resolution would be increased and the synchronizer wouldn't be needed. Some precautions must be implemented in order to obtain accurate measurements, in particular, background lights and reflections have to be reduced to the minimum and the seeding particles have to be chosen carefully. In fact, the seeding particles have to reflect the light and have to follow the investigated flow field without affecting it, since the motion that would be detected is the seeding particle one. The conditions under which the motion of the particles follows the flow field are derived from the Basset equation

$$\left(\frac{\pi {D_p}^3}{6}\rho_p\right)\frac{du_p}{dt} = 3\pi\mu_a D_p(u-u_p)$$

$$\frac{du_p}{dt} = \frac{18\nu_a(u-u_p)}{{D_p}^2(\frac{\rho_p}{\rho_a})}$$

and are governed by: the ratio between the "material density" of the particles ρ_p and of the flow field, for example air density ρ_a, which must be about one. If this were not the case, fictitious velocity would be introduced, these would be given by a buoyancy effect for $\frac{\rho_p}{\rho_a} < 1$ or by a "sinking effect" for a ratio greater than one. Another seeding parameter that affects the flow field is the size of the particles: too small particles would reflect the light poorly while too big ones would have too much inertia following the flow field. For instance, for the air, the order of magnitude of the seeding particle diameter is of a few microns. The dimensionless parameter that comes out from the Basset equation and that summarizes the above relations is the Stokes number

$$St = \frac{t_p}{t_0}$$

where t_0 is a characteristic time of the flow field while t_p stands for relaxing time and is the reaction time of the particles under the effect of the motion field through the viscous forces acting on the particles themselves. This relaxing time is given by the above-mentioned parameters that characterized the choice of the right particles for seeding purposes

$$t_p = \frac{D_p^2\ \rho_p}{\mu_a}$$

The conditions under which the particles follow the flow field without altering is the following:

$$St <<< 1$$

As can be seen in Figure 4.14, generally a raw PIV snapshot seems to be an ensemble of enlighted dots in a dark background. In a post-processing phase, for a non-time resolved and single exposed planar PIV, from a couple of PIV snapshots time separated by an hardware imposed Δt, it will be obtained an instantaneous velocity field.

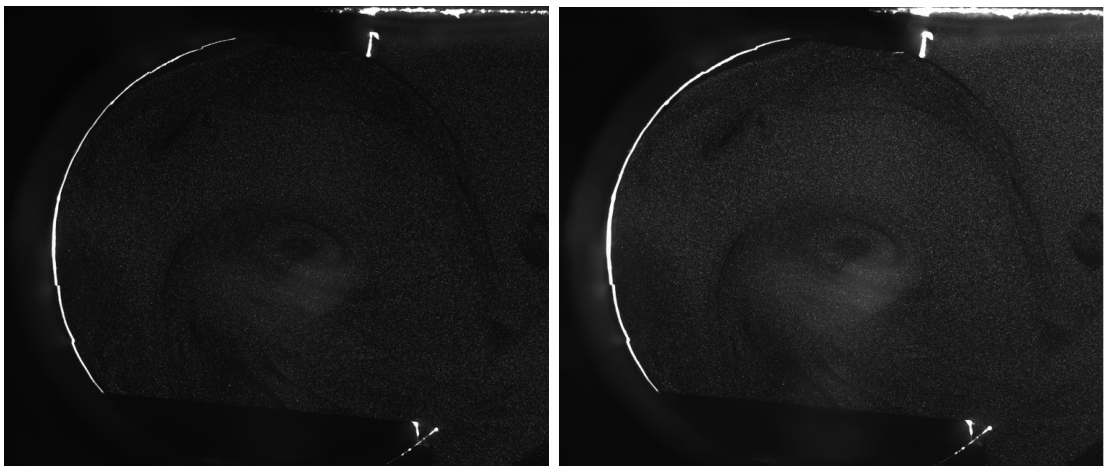

Raw PIV snapshot at time t. Raw PIV snapshot at time $t + \Delta t$

Figure 4.14: Couple of PIV images for a non-time resolved and single exposed planar PIV over the sample test ($t = 1.25\ mm$) in quiescent air at operating condition $f = 12\ kHz$, $V = 12\ kV$.

Each digital image is discretized as a map of numbers between 0 and $2^{\#bit}$ representing the light intensity of each pixel of the field of view, discretized as a gray scale with a number of levels depending on the number of bit of the camera used to take the PIV images. The displacement $\vec{\Delta}s$ missed to build a single velocity vector (Δt is imposed by the user under set up limitation) $\vec{V} = \frac{\vec{\Delta}s}{\Delta t}$ is estimated through some post-processing algorithms that partition the space resolution of the digital images in smaller interrogation windows, usually square shape (Δh [px] x Δk [px]), and on each of them, for the couple of PIV images, are calculated the cross-correlation function of the intensity levels ($f(h,k)$) in the same interrogation area but in the two images separated by a Δt.

$$R_{j,j+1}(r_1, r_2) = \sum_{h=1}^{\Delta h} \sum_{k=1}^{\Delta k} f_j(h,k)\ f_{j+1}(h + r_1, k + r_2) \Delta h\ \Delta k$$

The peaks of the cross-correlation function identifies the point of maximum probability defined by the distance from the origin and the centroid of the maximum intensity peak. This distance is the estimated $\vec{\Delta s}$ that, coupled with the imposed Δt will give a velocity vector in $px\ s^{-1}$ dimension. To move on to the physics dimension, i.e $m\ s^{-1}$, it simply needs to correlate the px x px dimensions to a real dimension of the field of view, for instance, just recording or taking a picture of an object, scale, of known dimension. Iterating the same process through the whole image, then for each interrogation area, it will be mapped the velocity vector field. In addition to the previously exposed precautions and a needed homogeneous seeding, there are also some on the interrogation area and indeed Δt chosen, in fact, some empirical rules are given: each single interrogation area has to be filled with almost ten particles and the dimension of the interrogation window must be such that the particles within it are the same ones framed by the same interrogation area time-spaced apart by a Δt. This restriction is motivated by the fact that the particles coming in and leaving each interrogation area in a time step Δt have to be limited to the minimum or in any case confined to the edges of the interrogation area. To do not lose the cross-correlation, indeed the motion, of the particles on the edge of the interrogation area it is usually implemented an overlapping part between two adjacent interrogation areas that it will result in a sort of spatial interpolation between the velocity vectors of the two. The empirical rule that guarantees a limited number of particles coming and leaving each window in a Δt is that the displacement traveled by the particles in a time step has to be approximately equal to a third of the interrogation windows' length. Generally, to obtain a more accurate estimation of the velocities vector more of the above exposed iterating processes are done, in particular, the iterations are done refining the interrogation windows so that the step with the coarse grid can capture the order of magnitude of $\vec{V}$ while the following steps will capture the smaller orders $\Delta\vec{V}$. Hence, the empirical rule over the displacement traveled by the particles in a time step has to be imposed over the size of the coarse grid of interrogation windows. This multi-step method is the one implemented in the code used to obtain the results that are going to be presented in this chapter.

At the conclusion of this brief PIV overview it is in the writer's interest to underline how some pre-processing can be implemented too, in particular a sort of mask, or rather a region of the field of view where we are not interested in or that we know that there aren't flow stream, i.e. solid body, and that we are gonna obscure placing the value at 0 (black) in the grayscale. This is made with the purpose of reducing the processing time. Raw PIV snapshots usually pass through a further pre-processing method known as Proper Orthogonal Decomposition (POD) that after a modal spatial decomposition of all set of images, search for energy peaks that repeat themselves in all the images and therefore don't change in time, subtracting

them from the images. This is implemented in order to not take into account the intensity peaks that do not change in time, indeed not due to the motion of the seeding particles but for example to some reflections that have not been physically eliminated, that may affect the measurements.

4.2.2 Experimental set up.

The following results are obtained through a not time-resolved planar PIV with single exposition, in quiescent air. The seeding particles used to seed the flow field inside a glass case are PIVLIGHT (PIVTEC GmbH).
The experimental setup sketched in Figure (4.15) comprehends: a laser source (Dantec Dynamics 15 Hz, 200mJ/pulse laser), a mirror to deflect the laser ray, a spherical lens (LA1908-ML f=500.0 mm) and a cylindrical one (LK 1336-RM f=-50.00 mm) to open it up and generate a thin laser plane, a sCMOS camera (Andor Zyla High resolution 5.5 MP sCMOS 2560 x 2160 px sensor) placed perpendicularly to the laser sheet and a synchronizer system to simultaneously acquiring the images while emitting the laser beam.

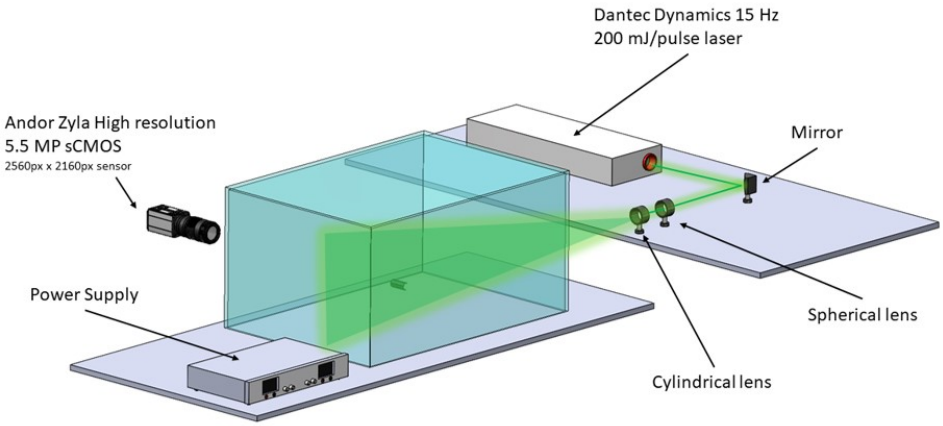

Figure 4.15: Sketch of the PIV set up.

The instruments to generate a high voltage - high frequency signal for plasma generation (Figure 4.6), the function generator, the power supply, and the oscilloscope (Figure 4.5) like the "open short pipe" sample (Figure 4.1) and the three DBD-PAs dimensions (Table 4.1) are the same of Section 4.1. The sampling frequency is $f_s = 15\ Hz$ and indeed the time resolution, or rather the time intervals between each couple of snapshots is $\Delta T = \frac{1}{f_s} = 0.0667\ s$ while the physical field of view dimensions are about 32 x 27 mm which lead to having 80 px/mm. The density of velocity vectors for the following results is about 24 vectors/mm^2.

4.2.3 PIV results and post-processing.

The PIV measurements carried out in this project are aimed to extract a fluid dynamic effect to characterize mechanically the DBD-PAs mounted on a cylindrical surface using PLA wall as a dielectric material. As declared in Chapter 1 the final design presents four DBD-PAs placed cardinally along the streamwise direction, hence each PA will be affected by the presence of the previous one and will affect the following one in tangential direction. Since for optical reasons the test sample of this PIV campaign must have an open section, we have the possibility to place only three DBD-PAs and the only one that presents the final design condition is the central one which sees one PA before and one after in tangential direction. For these reasons, in the following, we will focus on that one.
As the first try it was tested a C section with 180° of the cylindrical wall, or rather half of the pipe, this test sample allows illuminating all the PAs with the laser sheets, thus it's possible to see the flow field around all the PAs. Unfortunately due to the geometric characteristic only two DBD can be mounted, and the mass entrainment of the one upstream has the same topology observed of the DBD-PAs mounted on a flat surface, therefore how it will be observed in the following, this isn't the behavior that we will be expected in the closed final configuration. For these reasons this design of the test sample was discarded and more than 180° of the wall was taken into account.This change in test sample's design leads to a different mass entrainment behavior but have the drawback that one of the two PAs placed on the edges is not hit by the laser sheet due to the shadow of the PLA wall, therefore a region of flow field will be missed but the central actuator will still be affected by the jet stream of the shadowed one. The test case is the same as Table 4.4 and indeed it will be possible to couple the electrical power consumption to the mechanical characterization in order to obtain an estimation of the efficiency.

Results

The following results are the mean fields of three hundred instantaneous velocity fields each described by a coupled of PIV images pre-processed with five modal POD analysis and separated by a $\Delta T = \frac{1}{f_s} = \frac{1}{15\ Hz} = 0.0667\ s$ while the Δt that separates the images of each couple, thus the Δt used to compute the velocity vectors is $\Delta t = 500\ \mu s$. The code for the post-processing of the PIV analysis has been provided only as a user while the source code is hidden and it wasn't developed by the writer; for this reason a detailed analysis of the code it's not the subject of this work. However, it's important to underline how the code works better for high values of windows overlapping and that the quality of the computed vectors is checked through a median test [23]. The parameters about overlapping

and window sizes in the multi-step process chosen as well as some of the already mentioned specifications are reported below:

- $\Delta t = 500\ \mu s$.
- Pixel to millimeters ratio: $80\ px \cdot mm^{-1}$.
- Camera sensor: $2560\ x\ 2160\ px$.
- Multi-step windows size ($l\ x\ l$): $l = 64,\ 32,\ 16\ px$.
- Windows overlap: 50%.

The flow fields expressed with a polar system of reference with the origin in the center of the virtual cylinder, in particular tangential (V_θ) and radial (V_ρ) for the test cases are reported below.

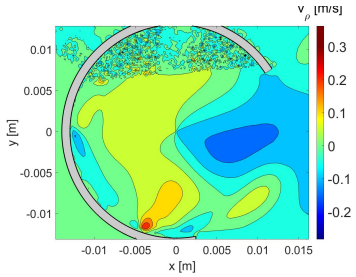

Radial velocity field V_ρ.

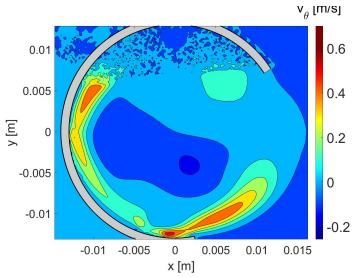

Tangential velocity field V_θ.

Figure 4.16: Velocity interpolated fields at operating condition: $V_{pp} = 10\ kV$, $f = 12\ kHz$ with a dielectric thickness $t = 1\ mm$

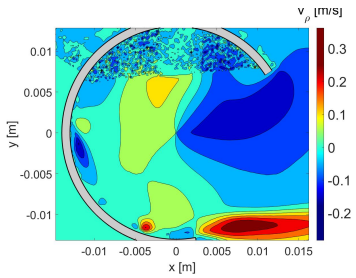

Radial velocity field V_ρ.

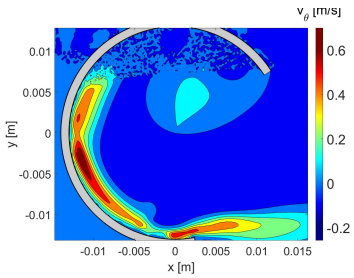

Tangential velocity field V_θ.

Figure 4.17: Velocity interpolated fields at operating condition: $V_{pp} = 11\ kV$, $f = 12\ kHz$ with a dielectric thickness $t = 1mm$

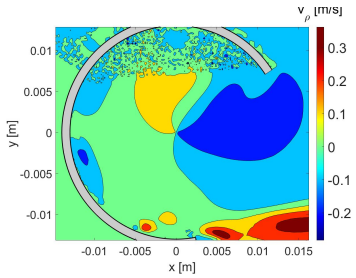

Radial velocity field V_ρ.

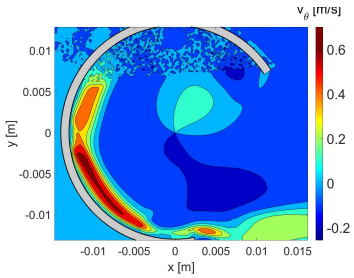

Tangential velocity field V_θ.

Figure 4.18: Velocity interpolated fields at operating condition: $V_{pp} = 12\ kV$, $f = 12\ kHz$ with a dielectric thickness $t = 1\ mm$

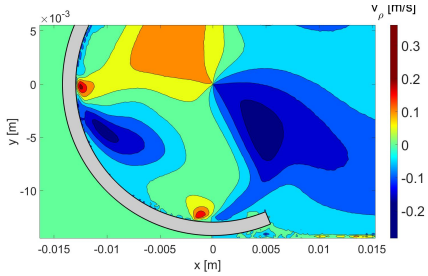

Radial velocity field V_ρ.

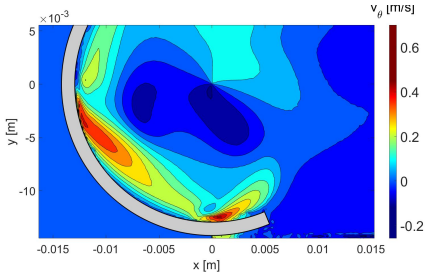

Tangential velocity field V_θ.

Figure 4.19: Velocity interpolated fields at operating condition: $V_{pp} = 10\ kV$, $f = 12\ kHz$ with a dielectric thickness $t = 1.25\ mm$

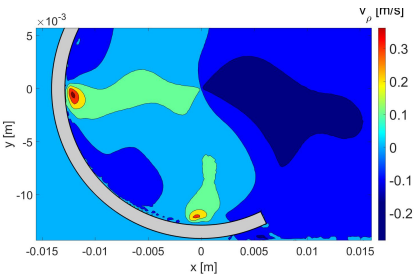

Radial velocity field V_ρ.

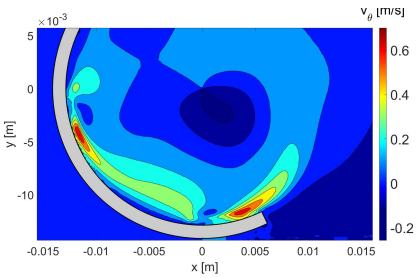

Tangential velocity field V_θ.

Figure 4.20: Velocity interpolated fields at operating condition: $V_{pp} = 11\ kV$, $f = 12\ kHz$ with a dielectric thickness $t = 1.25\ mm$

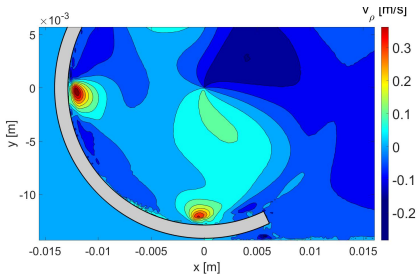

Radial velocity field V_ρ.

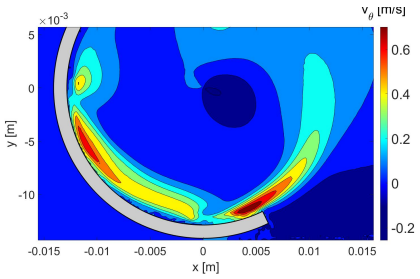

Tangential velocity field V_θ.

Figure 4.21: Velocity interpolated fields at operating condition: $V_{pp} = 12\ kV$, $f = 12\ kHz$ with a dielectric thickness $t = 1.25\ mm$

In Table 4.5 are reported the maximum tangential velocities relative to the central PA for each case. As expected, the maximum is given for the thinner PLA thickness at the highest voltage. Therefore the order of magnitude is the same and very low and it may predict a poor control authority for the Chapter 1 purpose, hence a limited range of operation for this proof of concept is expected.

$t_{diel} = 1\ mm$		$t_{diel} = 1.25mm$	
V_{pp} [kV]	$V_{\theta max}$ [m/s]	V_{pp} [kV]	$V_{\theta max}$ [m/s]
10	0.399	10	0.411
11	0.689	11	0.688
12	0.6267	12	0.682

Table 4.5: Maximum tangential velocities for each test case.

Moreover from Figure 4.16 to 4.18 it is notable how the topology of the jets of the PA placed downstream changes within the operating voltage. This phenomenology can be due to the fact that for higher voltage the injection of momentum operated by the DBD-PA overcomes the pressure gradient induced by the portion of the wall downstream of it. In particular, it also can be seen how for lower V_{pp} the flow field seems to create a sort of shear layer that seems to close the virtual cylinder.

In Figure 4.22 -4.23 are represented the trends of maximum tangential velocities along θ for the different operating conditions

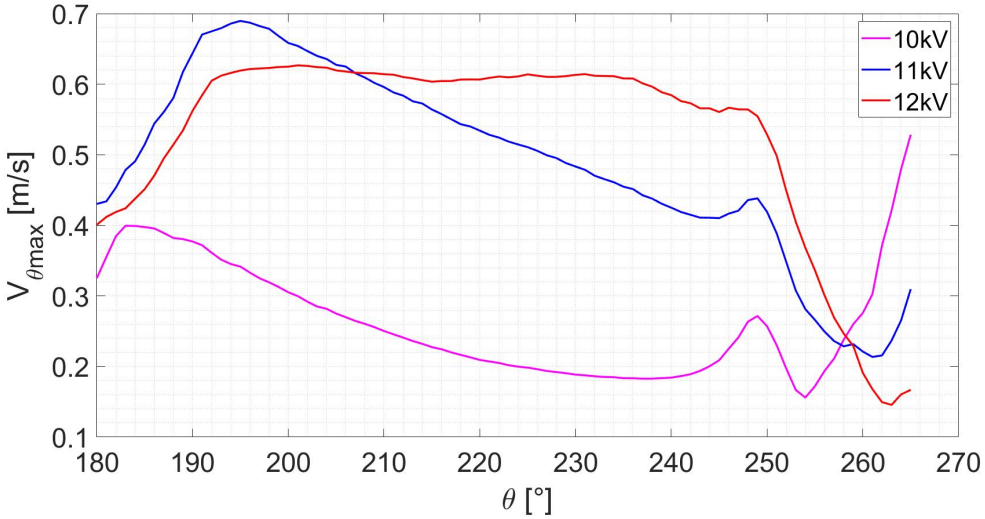

Figure 4.22: $V_{thetamax}$ trend along θ coordinate for the three operating voltage ($t_{diel} = 1\ mm$)

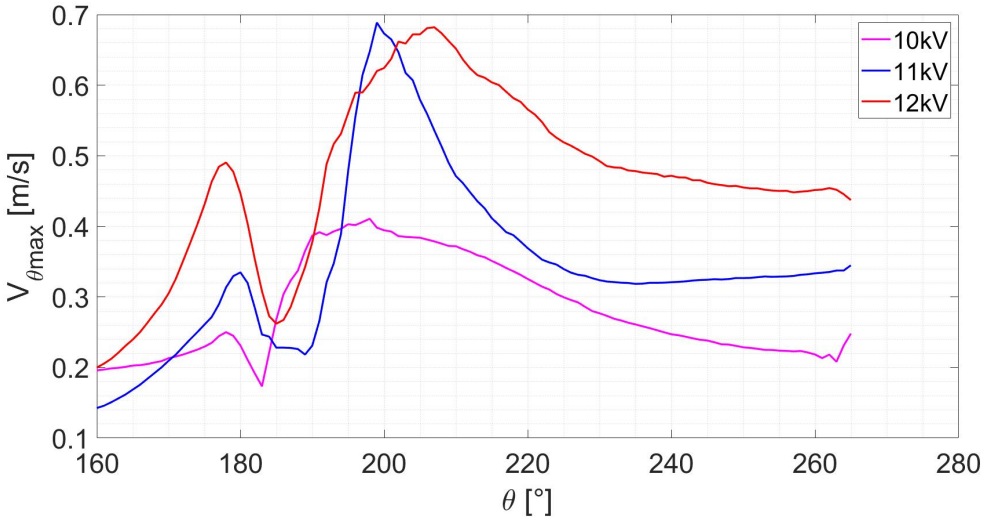

Figure 4.23: $V_{thetamax}$ trend along θ coordinate for the three operating voltage ($t_{diel} = 1.25\ mm$).

Moreover the V_θ profiles at a sampling θ position are reported in Figure 4.24-4.25 for each operating voltage. As the grid of interrogation areas of PIV multi-step process, hence the resulting velocity vectors are the ones of a cartesian reference system while the velocity profiles are reported in a polar one the number of points

of the interpolation is chosen of the same space resolution order of the optical measurements: about 60 velocity vectors along the inner radius ($r_{in} = 12.7\ mm$).

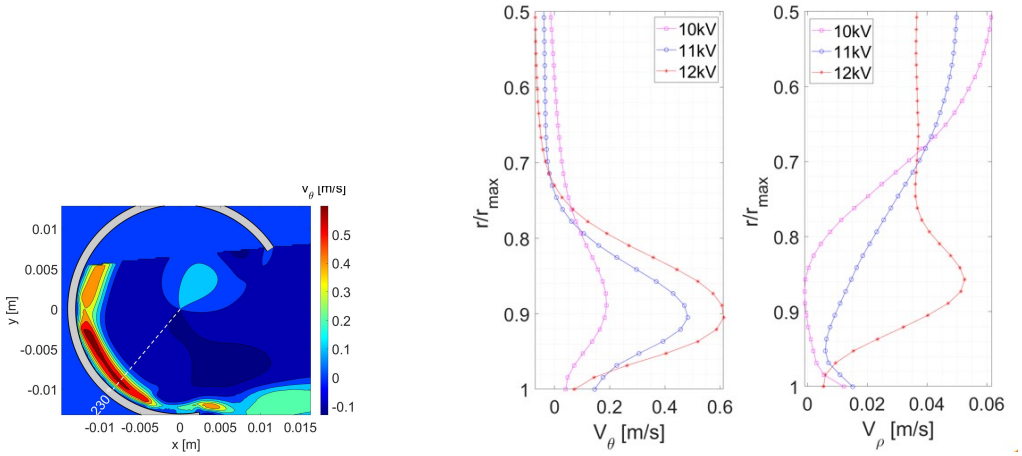

Figure 4.24: Velocity profile at $\theta = 230°$ for the three operating voltage ($t_{diel} = 1\ mm$)

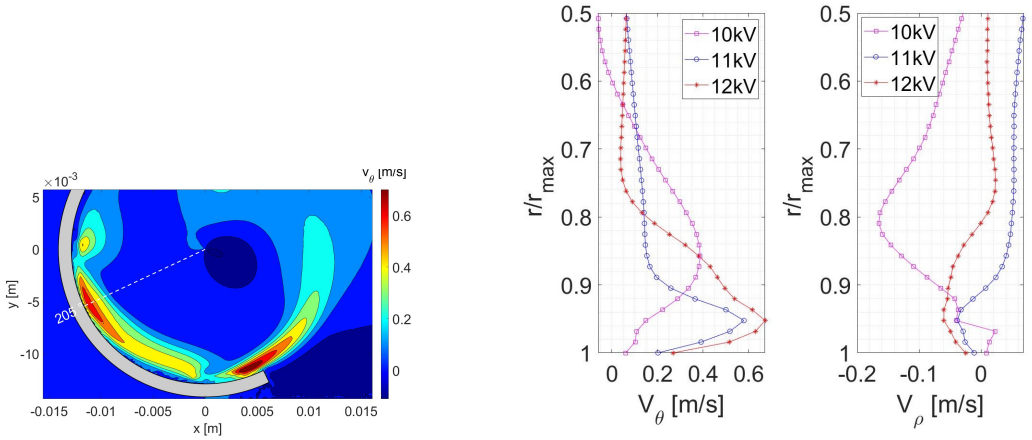

Figure 4.25: V_{theta} profile at $\theta = 205°$ for the three operating voltage ($t_{diel} = 1.25\ mm$).

The writer intends to underline how differences for the two dielectric thickness cases could be caused also by the not same "θ-positioning" between the test samples due to the manual setup of the two.
Trying to give a quantitative measure of the mechanical effect of the central PA as universal as possible, in the operating condition tested, starting from the output of the PIV mean flow fields the convective parts of the Navier-Stokes equation had

been computed. The results are limited to the convective parts by the fact that the flow fields are the time-averaged of 300 instantaneous and non-continuous fields, and therefore the hypothesis of time-independency has to be imposed as well as the real body force introduced by PAs couldn't be spun off by the contribute of the pressure gradient and wall effects, thus they are not computable individually.

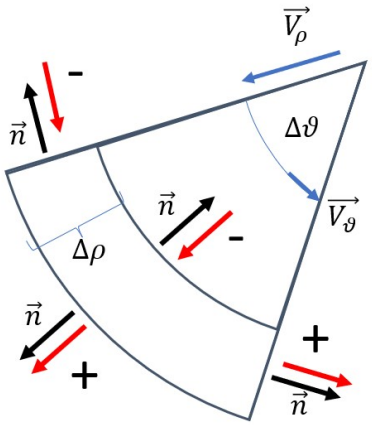

Figure 4.26: Moving control volume with the reference system, and wall normal direction.

To extract the above-mentioned mechanical effect of the main actuator a stretched control volume was implemented (Figure 4.26). The control volume is stretched by a small $\Delta\theta$ interval in an iterating process that allows to estimate the balance of convective quantities that enter and leave the control volume. With a radial spacing able to enclose all the central actuator's induced wall jet, expanding the control volume along the θ direction and imposing a quiescent air condition in the shadowed region, the trends along θ of the convective part of mass, $\rho-$momentum, $\theta-$momentum and energy had been computed (Figure 4.27). In particular, studying the $\theta-$momentum, it was possible to localize the region where the flow accelerated, positive derivative, thus where the effect of the PA's body force overcomes the friction and viscous effects. As mechanical output, it was chosen the jump between the peaks of energy trend and the lower value of energy corresponding to the entrainment zone of the downstream PA.

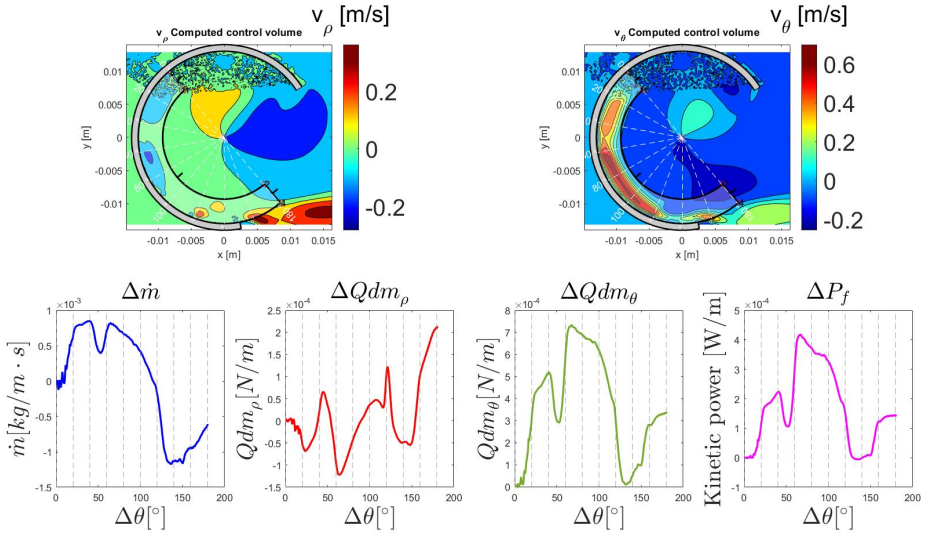

Figure 4.27: Trends of convective quantities of N-S equation for $t_{diel} = 1\ mm$, $V_{pp} = 12\ kV$

The mechanical outputs for each test case are given in Table (4.6) that with the previous electrical characterization results (Table 4.4) considering a constant mechanical effect along the axial direction, allow computing the efficiency.

$$\eta = \frac{P_f \cdot L_{plasma}}{P_A/3}$$

$t_{diel} = 1\ mm$		
$V_{pp}[kV]$	$P_f[W/m]$	η
10	$7.3567 \cdot 10^{-5}$	$1.42 \cdot 10^{-3}$
11	$4.2591 \cdot 10^{-4}$	$6.39 \cdot 10^{-3}$
12	$4.2511 \cdot 10^{-4}$	$4.91 \cdot 10^{-3}$
$t_{diel} = 1.25\ mm$		
10	$9.44740 \cdot 10^{-5}$	$3.24 \cdot 10^{-3}$
11	$1.90278 \cdot 10^{-4}$	$4.66 \cdot 10^{-3}$
12	$3.51708 \cdot 10^{-4}$	$6.30 \cdot 10^{-3}$

Table 4.6: Estimated mechanical characterization and efficiency.

As last PIV test, and only as qualitative result and outlook aim, is reported a test over a closed short pipe with four DBD-PAs ($t_{diel} = 1\ mm$). This PIV measure saw the laser sheet hit perpendicularly to the axial direction right downstream of

the exit section of the pipe, from where the seeding flow was coming out with a low velocity not pneumatically detectable. The non-quantitative nature of these results is due to the fact that the box placed upstream of the flow used to enclose the seeded flow, wasn't a stagnation chamber, and the measure it will be affected by the non-detected out-of-plane motion that, even if it was low, could decouple the particles recorded in the PIV snapshots at t and $t + \delta t$ belonging to each couple.

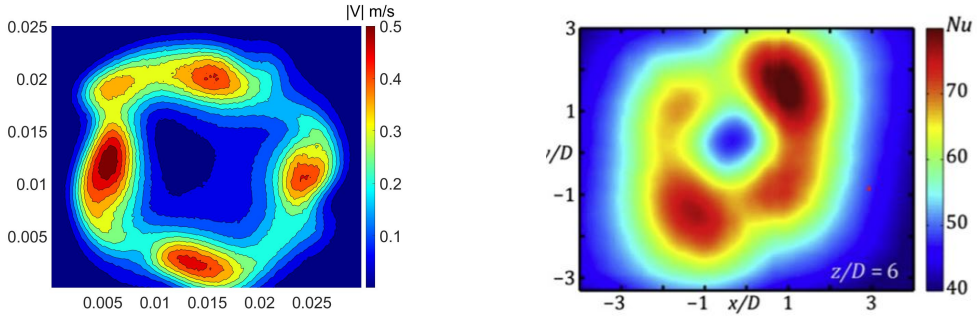

(a) (b)

Figure 4.28: PIV measurement at $V_{pp} = 12\ kV$, $f = 11\ kHz$ (with $\Delta t = 500\mu s$ and a calibration factor of 85.33 px/mm) (a) and (b) a Nusselt number distribution of a multichannel impinging swirling jet [4]

Keeping an eye on the topology of the flow field they can be identified four regions of greater tangential velocities caused by the operating DBD-PAs. These regions, seem very similar to the ones obtained through the IR technique by Ianiro et al [4], however with the due differences in technique, accuracy, quality, physics principle, and jet configurations behind the two.

Chapter 5

Passive swirl measurements

5.1 Jet facility.

The jet facility available at the Polytechnic University of Turin aerospace department's laboratory Modesto Panetti is a subsonic jet with a polynomial profile with tangent imposed inlet and outlet convergent nozzle of one-inch exit diameter. It is flanged through six bolts to a cylindrical section of 79.15 mm inner diameter. The pneumatic line sees a maximum of 8 bar then two controlling valves one with the largest pressure losses and coarse control and the latter with a fine pressure control reduce it. The facility is safe to use at a maximum of 2 bar and it was projected to generate also heated jet with a thermo-couple placed in it and a series of filters for humidity control. A CAD section of the nozzle is reported below (figure 5.1).

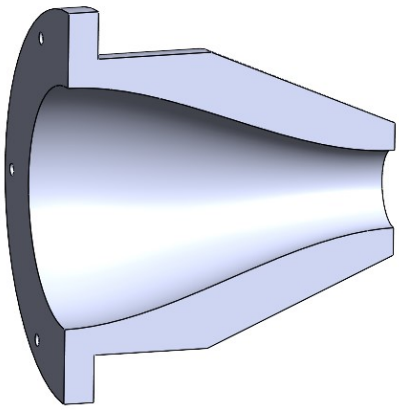

Figure 5.1: Section of a nozzle's sketch

For the thesis project it was necessary to have the availability to mount various insets downstream of the nozzle: without any possibility to operate on the present nozzle, due to its brittleness, it was decided to couple through six threaded rod an inset with the same flange dimension of the nozzle where, inside, they can be placed various insets like a short pipe, for free jet case, and different passive and active swirling insets, adding versatility to the facility. In the figure below shown the CAD model of the flange (Figure 5.2) and the exploded view (Figure 5.3) of the setup from the convergent nozzle already present in the jet facility to the short pipe inset.

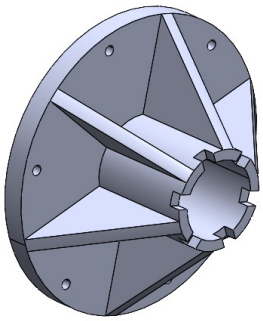

Figure 5.2: CAD model of the flange support.

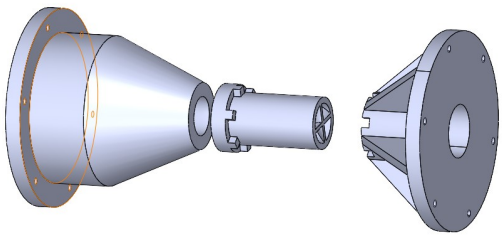

Figure 5.3: Exploded CAD view from the nozzle to the inset and its support.

It was chosen to make insets and the flange support through the 3D printer available at the department (Raise 3D pro), this choice is justified by the possibility of overcoming the eventually delivery time needed to commissioning the parts to privates companies and by the preliminary nature of the studies carried out in this project.

5.2 Five-hole probe calibration.

For the pneumatic measurements, due to the three-dimensional characteristic of a swirling jet, it was chosen an axial five-hole probe which, after calibration, can guarantee three outputs: magnitude of the velocity and two directional angles in perpendicular planes. In particular, this probe (Figure 5.5a) has a spherical head of 0.5 cm diameter with four directional static pressure holes and a central total pressure hole. The four directional holes, placed in two perpendicular planes are responsible for the two angular outputs while the total pressure hole is of the magnitude of the velocity vector.
Before getting into the calibration process it's useful to define the probe's system of reference which sees a ternal cartesian system (Figure 5.4) centered in the probe's head with the X axis along the axial probe's dimension coming out of the head, Z axis pointing upwards while Y axis completes the right-handed system. As a numbering reference it was chosen the one illustrated in the Figure 5.5b that looked from behind saw the following numbering for the pneumatic lines with their respective holes.

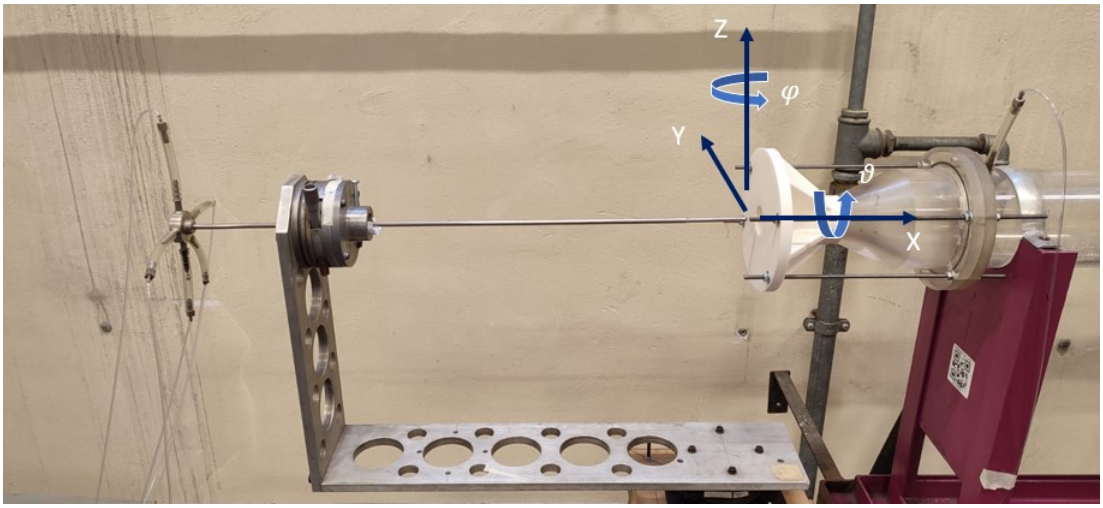

Figure 5.4: Reference system.

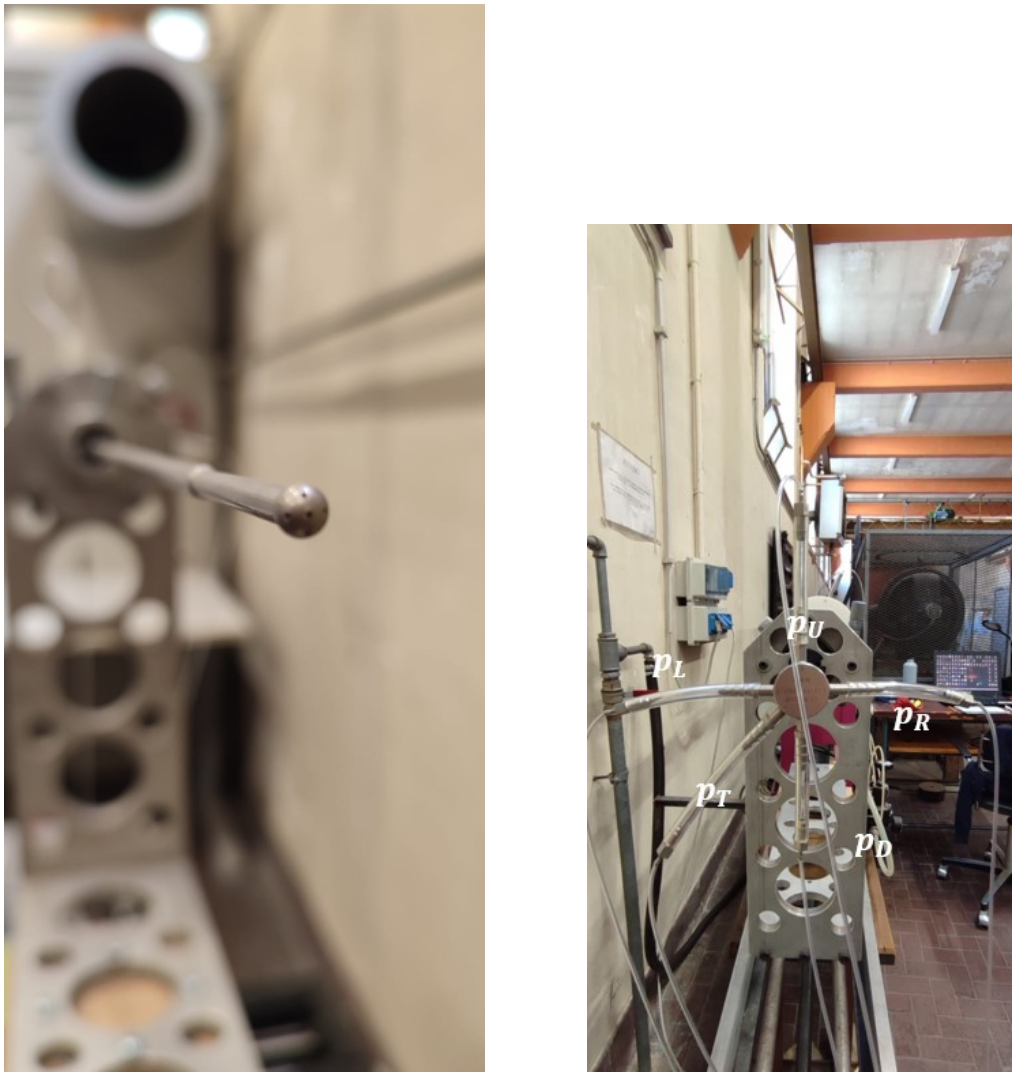

(a) View of the probe's head. **(b)** Numbering of the pressure lines.

Figure 5.5: Frontal view of the probe (a) and numbering of the pressure line (b)

- $p_1 = p_D$: down (towards negative Z)
- $p_2 = p_T$: total pressure
- $p_3 = p_U$: up (towards positive Z)
- $p_4 = p_L$: left (towards positive Y)
- $p_5 = p_R$: right (towards negative Y)

In this calibration process, the probe was mounted on a steel L support with two rotating degrees of freedom (DoF): one around the X-axis and one around the Z-axis: θ and φ respectively. Both of them were taken positive if counterclockwise (Figure 5.4). These rotating DoFs aren't the most comfortable for this probe's calibration but were the only available; due to that, starting from θ and φ, it was necessary to compute some trigonometric transformations to obtain the α and β angles, in the XZ and XY planes respectively (Figure 5.6). To be more accurate, α is the angle between the flow direction and the axial probe axis, β instead is formed by the flow direction and the Y axis. For instance, the system of reference chosen leads to: in case of flow direction with $\alpha > 0$ causes a $p_1 > p_3$ while for $\beta > 0$, it will result in $p_5 > p_4$. Starting from the probe's reference system illustrated in Figure

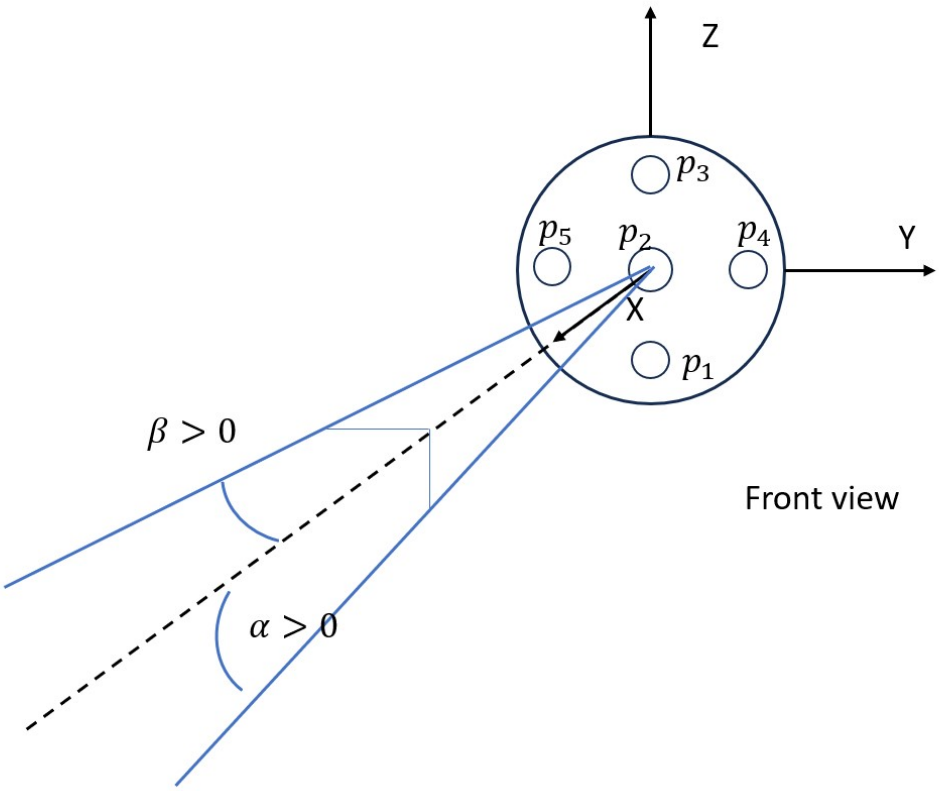

Figure 5.6: Sketch of the front view of probe's reference system.

5.7 and rotating around the Z axis (φ angle) the relative velocity components in

the new reference system X'Y'Z' (Figure 5.8) become:

$$\begin{aligned} u' &= u\cos\varphi - v\sin\varphi \\ v' &= u\sin\varphi + v\cos\varphi \\ w' &= w \end{aligned}$$

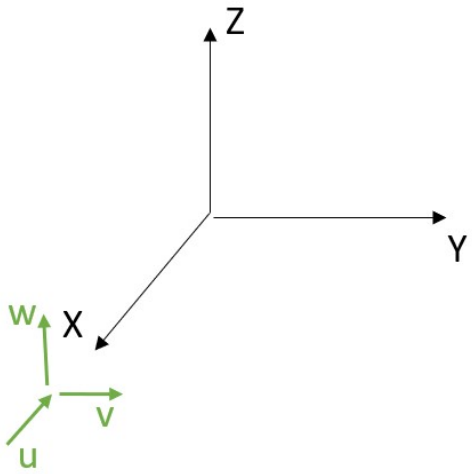

Figure 5.7: Probe's reference system with $\varphi = \theta = 0°$

Now rotating around X' (Figure 5.9) the relative velocity components become:

$$\begin{aligned} u'' &= u' \\ v'' &= v'\cos\theta + w'\sin\theta \\ w'' &= -v'\sin\theta + w'\cos\theta \end{aligned}$$

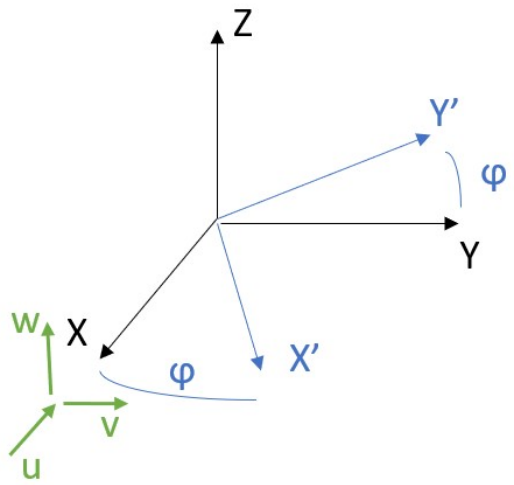

Figure 5.8: Probe's reference system with $\varphi \neq 0°$, $\theta = 0°$.

assuming to be in the center of the outlet in the potential core region (our calibration position), the velocity vector will present only the u component, so the relative velocity will be given only by that:

$$
\begin{aligned}
u_s &= u'' = u\cos\varphi \\
v_s &= v'' = u\sin\varphi\cos\theta \\
w_s &= w'' = -u\sin\varphi\sin\theta
\end{aligned}
$$

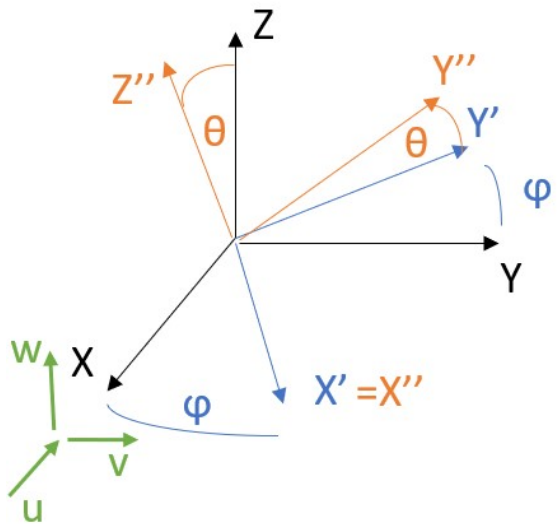

Figure 5.9: Probe's reference system with $\varphi \neq 0°$, $\theta \neq 0°$.

due to these trigonometric transformations, α, and β will be given by:

$$\alpha = \tan^{-1}\left(\frac{w_s}{u_s}\right) = \tan^{-1}\left(-\frac{\sin\varphi\sin\theta}{\cos\varphi}\right)$$

$$\beta = \tan^{-1}\left(\frac{v_s}{u_s}\right) = \tan^{-1}\left(-\frac{\sin\varphi\cos\theta}{\cos\varphi}\right)$$

5.2.1 Experimental set up.

The experimental set up (Figure 5.10) is composed by the jet facility with a circular short pipe inset placed after the convergent nozzle, the axial probe mounted on the aforementioned support equipped with two goniometers with the respectively rotation axis intersecting in the probe's head. The whole support has also a translation degree along the X-axis thanks to a manual carriage. The pneumatic pressures have been acquired through a DSA scanivalve module (Figure 5.11a), powered by a power supply (Figure 5.11b) and linked through an ethernet cable to a laptop, while the environmental data have been acquired through the meteorological station of the laboratory. The differential pressures acquired simultaneously with the DSA module were six: the five from the axial probe (p_1, p_2, p_3, p_4, p_5) and one (p_6) coming from upstream of the convergent nozzle. As will be explained in the following section, the calibration process needs also some measurements of the "true" dynamic pressure that will be provided thanks to a Pitot tube mounted once

on the L-support rotated with a $\varphi = 90°$ through a 3D printed adapter, instead of the axial probe.

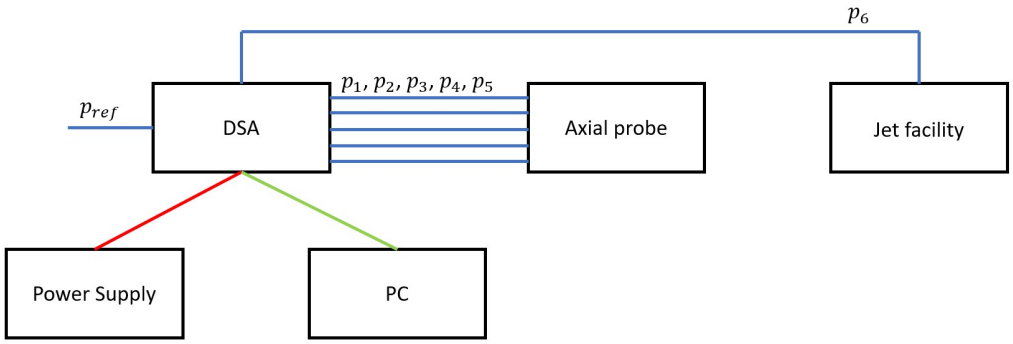

Figure 5.10: Sketch of the experimental set up.

(a) DSA module 3217/16px.

(b) Power supply KERT system 150/1.

Figure 5.11: DSA module (a) and his power supplier (b)

After the calibration phase, goniometer that gives the φ DoF was substituted by a horizontal motor driven carriage (Sigma Koki SGSP26-150) and a vertical manual one (THORLABS Lab Jack L490) that give the Y and Z translational DoF, respectively. So both, together with the manual carriage along the X direction, confer the completely translational tern of DOFs that will be exploited for the measurements in section 5.3

5.2.2 Logical process and calibration results.

First of all, to calibrate this particular probe it's important to define four dimensionless groups: two relative to directional angles α and β while the other two relative to total and dynamic pressure correction, however, all of them are α and β dependent.

- Sensibility in XZ plane (α):

$$f_\alpha = f_1(\alpha, \beta) = \frac{\Delta p_\alpha}{q} = \frac{p_3 - p_1}{p_T - p_M}$$

- Sensibility in XY plane (β):

$$f_\beta = f_2(\alpha, \beta) = \frac{\Delta p_\beta}{q} = \frac{p_5 - p_4}{p_T - p_M}$$

- Dynamic pressure correction:

$$f_3(\alpha, \beta) = \frac{q_{true}}{q} = \frac{q_{true}}{p_T - p_M}$$

- Total pressure correction:

$$f_4(\alpha, \beta) = \frac{\Delta p_T}{q} = \frac{p_T - p_{T0}}{p_T - p_M}$$

where p_T is the total pressure (p_2), q_{true} true dynamic pressure measured through a Pitot tube, p_{T0} the total pressure measured through the five-hole probe in the "0" position ($\alpha = \beta = 0°$) while p_M is the average of of the four "directional pressures".

$$p_M = \frac{1}{4}\Big(p_1 + p_3 + p_4 + p_5\Big)$$

Actually the pressures acquired with DSA were differential with respect to the environmental pressure but due to the fact that the dimensionless functions are differential too, so the environmental pressures cancel out.

First of all, to optimize the operative time, it was placed the Pitot tube in the central potential core region and acquired its two pressures, computed the dynamic pressure, useful to f_3 definition, and correlated the mean values with the mean values of p_6. It was noted that the points sampled stand in a straight line (Figure 5.12), so it was interpolated and obtained the equation that links p_6 to q_{true}.

Acquisition parameters and environmental data:

- $T_s = 25$ s
- $f_s = 20$ Hz
- $p_{amb} = 100400$ Pa
- $T_{amb} = 21.8°C$

Δp [bar]	0.2	0.4	0.6	0.8	0.9
$p_{Pitot} - p_{amb}$ [Pa]	0.6411	1.6857	4.6444	3.1070	2.3134
${p_{Pitot}}^0 - p_{amb}$ [Pa]	106.4440	171.3580	332.9405	472.3141	552.6226
$p_6 - p_{amb}$ [Pa]	105.7248	170.2513	330.8266	469.4639	549.4410

Table 5.1: Test matrix and mean data.

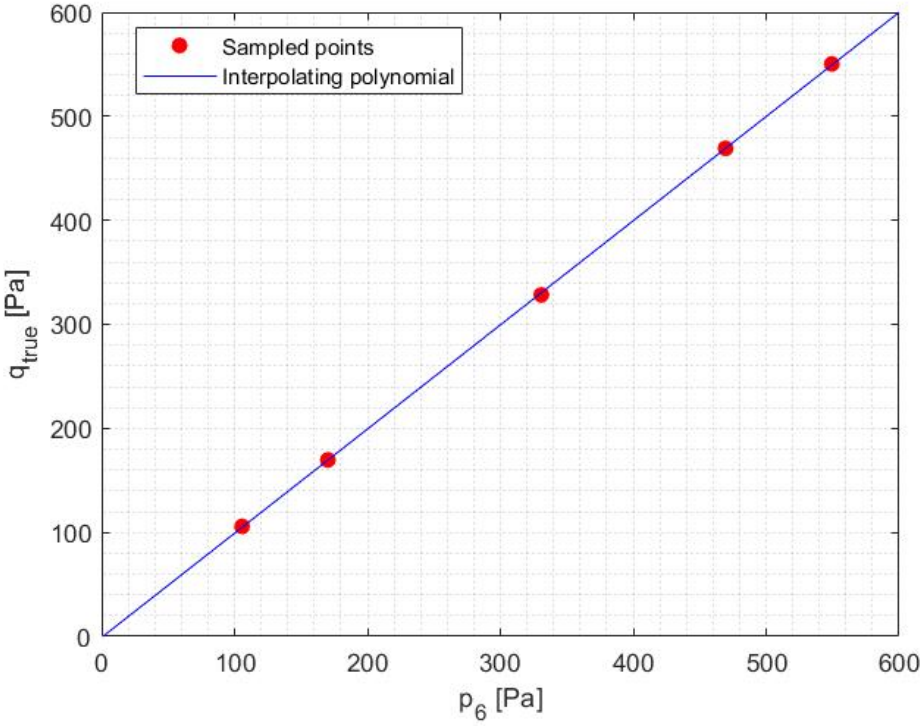

Figure 5.12: p_6 - q_{true} trend.

$$q_{true} = 1.0015 \cdot p_6 - 0.9738 \quad [Pa]$$

Stated the above relation useful to compute q_true without the physical change of probes, and mounted the axial probe, they have been acquired the six differential pressures varying θ from $-40°$ to $+40°$ with $10°$ steps for each φ from $-90°$ to $+90°$ with $15°$ steps , resulting in a 9x13 matrix. The sampling parameters, environmental data and delivery pressure were:

- $T_s = 15s$
- $f_s = 20Hz$
- $p_{amb} = 100000\ Pa$
- $T_{amb} = 22.9\ °C$
- $\Delta p = 0.4\ bar$

The sampled values of pressures acquired for each θ-φ position, corresponding to a α-β one, were averaged and then computed the f_1 and f_2 calibration functions. Using these computed values and the known angles $\alpha - \beta$, through a scattering

interpolation using Matlab function "griddata" were obtained two calibration maps (Figure 5.13) both with f_1 and f_2 on the axis that will be utilized in measurements to compute the unknown $\alpha - \beta$.

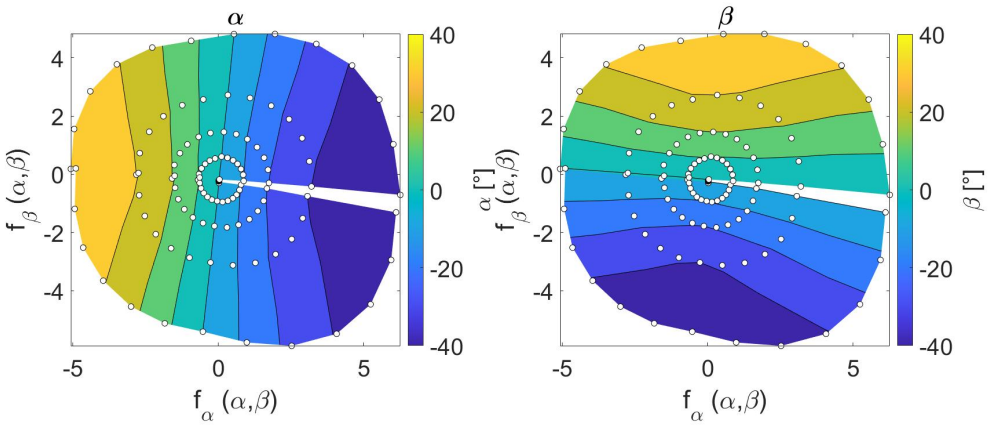

Figure 5.13: Calibration maps for α and β angles

It can be noticed that the maps weren't symmetrical in directions at all and that there is a missed data zone, these unexpected features are probably due to a probe's tilting or to misalignment and non-perfect intersection of rotational axis in the probe head, or both, that could cause a position shift varying θ-φ during acquisitions. These problems will be roughly overcome through another interpolation in the aforementioned zone. Obviously with the data acquired, and using the q_{true} relation from p_6 values, were also calculated f_3 and f_4, dynamic and total pressure correction respectively, and their interpolated maps. In the following measurements which will be presented, where, for instance, we will no longer be in a reference flow field nor α and β will be known, the logical steps that will be followed to obtain the local velocity vector starting from the pressures read by the DSA are:

1. Pressures detection through DSA module (five "probe pressures" and upstream pressure).

2. Averaging of the sampled values and computing f_{1M}, f_{2M}.

3. With the calculated dimensionless values f_{1M}, f_{2M} entering in the calibration map to obtain the couple α - β.

4. As long as f_3, f_4 are α and β dependent, starting from the, now, known angles the dynamic and total pressures can be corrected.

5. Through the environmental data the air density can be estimated, for instance, thanks to the ideal gas law, and the velocity magnitude can be obtained through the corrected dynamic pressure.

To ensemble all these steps it was created a Matlab function that receives in input, the file with pressures and environmental data and gives as outputs: α, β and $|\vec{V}|$. For instance, the velocity components (u, v, w) can be obtained starting from α, β and $|\vec{V}|$ through the following trigonometric relations:

$$u = \frac{|\vec{V}|}{\sqrt{1 + \tan^2\alpha + \tan^2\beta}}$$

$$v = u \tan\beta$$

$$w = u \tan\alpha$$

It is reported that the above equations are written under a difference reference system which from now it will be maintained, indeed X-axis is directed towards the opposite direction (entering the probe head) with respect the previous one, this change has the aim to consider the u component positive if coming out from the jet outlet. It is also relevant to specify that we will lose the right-handed nature of the reference system to pass to a left one.

5.3 Passive swirling jet measurements.

The geometry chosen for the passive swirling insets presents a cross swirling strips [4] (Figure 5.14) that force the flow to follow a helical path that causes the birth of a tangential motion. An empirical relation used to estimate the Swirl number (S) by geometrical parameters is given by Gupta et al.[1] and it's the following:

$$S = \frac{2\left[1 - \left(\frac{d}{D}\right)^3\right]}{3\left[1 - \left(\frac{d}{D}\right)^2\right]} \tan\theta$$

where D is the internal diameter, d the hub diameter and θ the swirl angle.

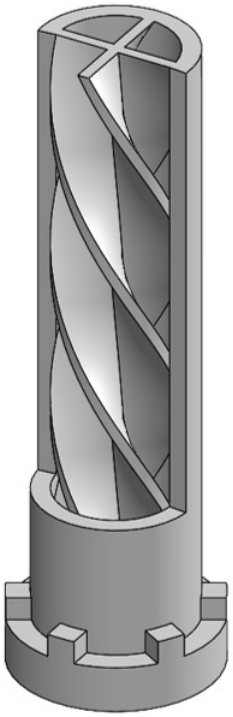

Figure 5.14: Example of the helicoidal inset CAD design.

For the 3D printed insets subject of this study: length, inner diameter, and hub diameter (so also the thickness of the strips) were kept fixed while the swirl angle was changed, varying the S desired. As the first output a partial YZ-plane flow field induced by a S = 0.4 insets was sampled at $f_s = 20\ Hz$, $T_s = 15\ s$ and $\Delta p = 0.4\ bar$ as reported in Table 5.2 - 5.3 and the interpolated V_θ mean fields are shown in Figures 5.15 -5.16. As previously remarked, due to the left-handed system of reference, V_θ is positive if clockwise with the X-axis coming out of the plane.

Z	y																		
0	-18	-16	-14	-12	-10	-8	-6	-4	-2	0	2	4	6	8	10	12	14	16	18
4.2	-18	-16	-14	-12	-10	-8	-6	-4	-2	0	2	4	6	8	10	12	14	16	18
7.45	-18	-16	-14	-12	-10	-8	-6	-4	-2	0	2	4	6	8	10	12	14	16	18
13.66	-18	-16	-14	-12	-10	-8	-6	-4	-2	0	2	4	6	8	10	12	14	16	18

Table 5.2: Test matrix [mm]: S=0.4 at X=1D ($f_s = 20\ Hz$, $T_s = 15\ s$ and $\Delta p = 0.4\ bar$)

Z	y																		
0	-18	-16	-14	-12	-10	-8	-6	-4	-2	0	2	4	6	8	10	12	14	16	18
4.2	-18	-16	-14	-12	-10	-8	-6	-4	-2	0	2	4	6	8	10	12	14	16	18
7.45	-18	-16	-14	-12	-10	-8	-6	-4	-2	0	2	4	6	8	10	12	14	16	18
13.66	-18	-16	-14	-12	-10	-8	-6	-4	-2	0	2	4	6	8	10	12	14	16	18

Table 5.3: Test matrix [mm]: S=0.4 at X=2D ($f_s = 20\ Hz$, $T_s = 15\ s$ and $\Delta p = 0.4\ bar$)

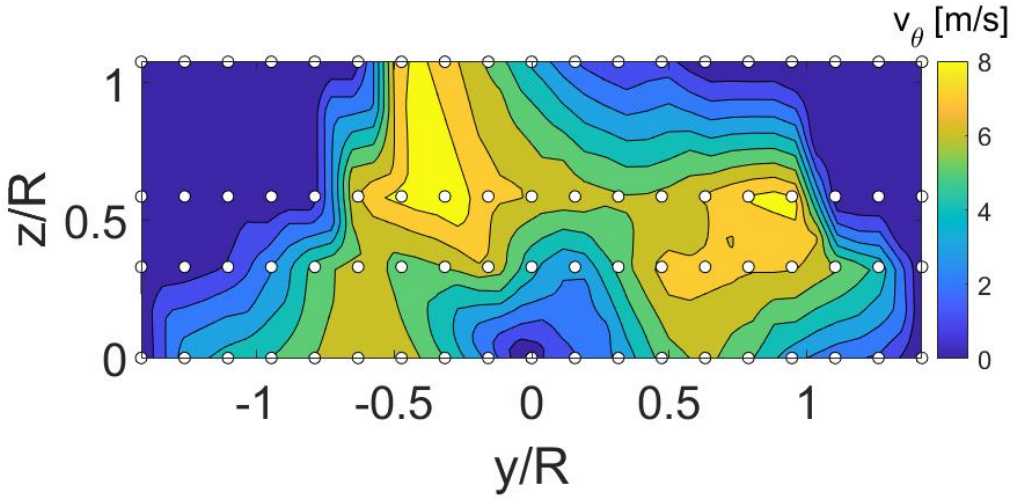

Figure 5.15: Half YZ planes at X=1D for S=0.4

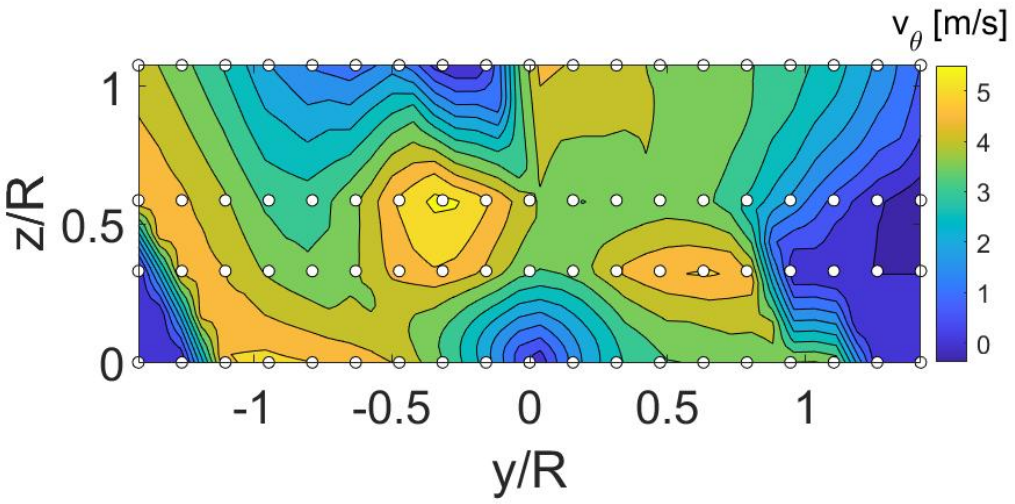

Figure 5.16: Half YZ planes at X=2D for S=0.4

Before showing some swirling flow field measurements more seeded with sampled points it's important to keep an eye on the statistical convergence because if in the calibration case, we were placed in the potential core of a circular free jet, the nature of a swirl jet flow field is completely different and for instance, it can be more "unsteady" and variable, so it could be worth to increase the sampled time while the frequency was maintained at 20 Hz due to DSA limitation (maximum 500 Hz accumulative per channel), thus due to the damping effect of the pneumatic lines. Despite the possibility of increasing the sampling frequency, the advantages are irrelevant since it would be still low and it would not allow making other statistical considerations and/or decomposition, for instance in order to evaluate

turbulent quantities that are not computable with this setup. To evaluate the statistical convergence, two sample positions of maximum (probably in a shear layer region) and minimum oscillation of the pressure values, and therefore measurement uncertainty, of the flow field presented in Figure 5.16 were identified through a propagation study of the standard deviation in the alpha and beta calculation process. At these positions (Table 5.4), five-minute acquisitions were made and the average trend over time of each pressure normalized by the average of each pressure value during all the sampled period are plotted in Figure 5.17.

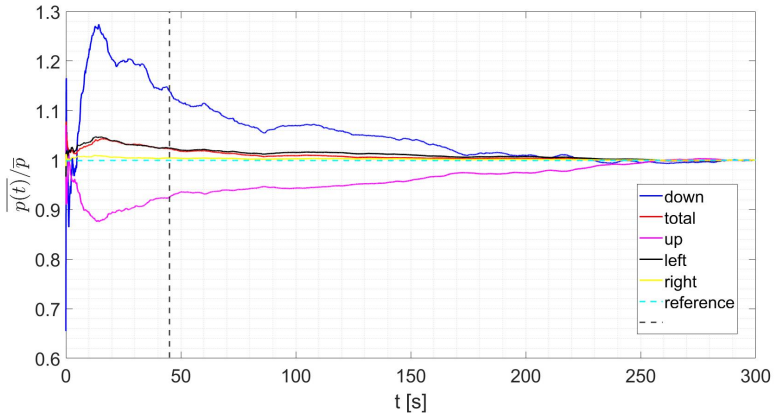

(a) X=2D, y=0, Z=4.2mm

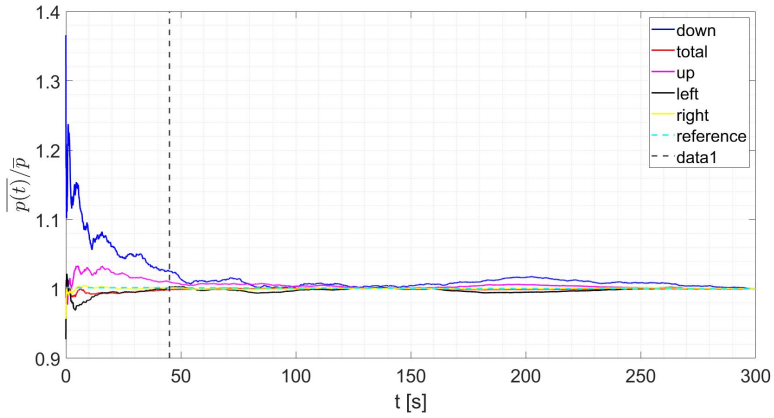

(b) X=2D, y=0, Z=7.45mm

Figure 5.17: Mean pressures at time t over mean along all sampling period for the position in table 5.4.

X	Y [mm]	Z [mm]
2D	0	4.2
2D	0	7.45

Table 5.4: Positions for a statistical convergence study.

As evident from the statistical trends of both cases, the sampling period must be increased, for further measurements an optimum value of $T_s = 45\ s$ has been identified.

From Figure 5.18a to 5.21 some V_θ mean fields (YZ planes) are shown each sampled at $f_s = 20\ Hz$ and $T_s = 45\ s$. For the $S = 0.2$ (Figure 5.18a-5.18b) and the three more distant from the exit nozzle $S = 0.1$ fields delivery pressure was set at $\Delta p = 0.2 bar$ and each field is characterized by 65 sampled points (Table 5.5 - 5.6).

Z[mm]	y [mm]												
0	-24	-20	-16	-12	-8	-4	0	4	8	12	16	20	24
7.65	-24	-20	-16	-12	-8	-4	0	4	8	12	16	20	24
11.1	-24	-20	-16	-12	-8	-4	0	4	8	12	16	20	24
13.95	-24	-20	-16	-12	-8	-4	0	4	8	12	16	20	24
-10.05	-24	-20	-16	-12	-8	-4	0	4	8	12	16	20	24
-16.6	-24	-20	-16	-12	-8	-4	0	4	8	12	16	20	24

Table 5.5: Test Matrix at X=2D , 3D for S=0.2

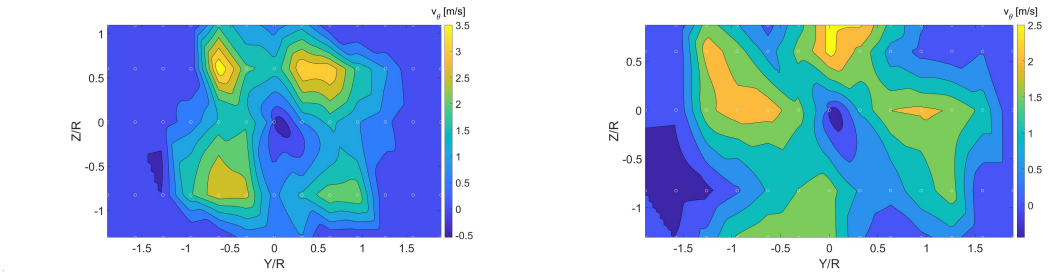

(a) **(b)**

Figure 5.18: Time-averaged interpolated V_θ field for S=0.2 at X=2D 5.18a and X=3D 5.18b

Z[mm]	y [mm]												
0	-24	-20	-16	-12	-8	-4	0	4	8	12	16	20	24
7.65	-24	-20	-16	-12	-8	-4	0	4	8	12	16	20	24
11.1	-24	-20	-16	-12	-8	-4	0	4	8	12	16	20	24
-10.05	-24	-20	-16	-12	-8	-4	0	4	8	12	16	20	24
-16.6	-24	-20	-16	-12	-8	-4	0	4	8	12	16	20	24

Table 5.6: Test Matrix at X=1D, 2D, 2.5D for S=0.1.

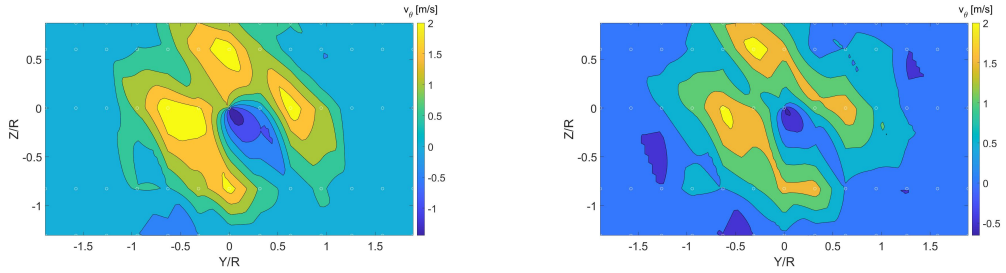

(a) **(b)**

Figure 5.19: Mean interpolated V_{theta} field for S=0.1 at X=1D (5.19a) and X=2D (5.19b)

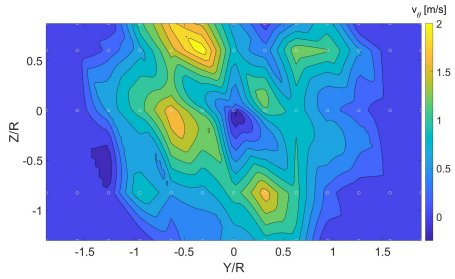

Figure 5.20: Mean interpolated V_{theta} field for S=0.1 at X=2.5D

Instead, as the last $S = 0.1$ field, a refined field was sampled with 200 sampled points (Table 5.7) in a YZ plane closer to the exit nozzle (X=0.5 D) with a delivery pressure that leads to a value of differential static pressure of $66Pa$ upstream the nozzle (p_6).

Z [mm]	-11.8	-9.15	-6	-2.95	0	3.1	6.45	9.5	11.35	12.6
	-7	-9	-13	-14	-14	-14	-13	-9	-7	-6
	-6	-8	-12	-13	-13	-13	-12	-8	-6.5	-5
	-5	-7	-11	-12	-12	-12	-11	-7	-6	-4
	-4	-6	-10	-10	-10	-10	-10	-6	-5.5	-3
	-3	-5	-8	-8	-8	-8	-8	-5	-5	-2
	-2	-4	-6	-6	-6	-6	-6	-4	-4.5	-1
	-1	-3	-5	-5	-5	-5	-5	-3	-4	0
	0	-2	-4	-4	-4	-4	-4	-2	-3.5	1
	1	-1	-3	-3	-3	-3	-3	-1	-3	2
	2	0	-2	-2	-2	-2	-2	0	-2.5	3
	3	1	0	0	0	0	0	1	-2	4
	4	2	2	2	2	2	2	2	-1.5	5
	5	3	3	3	3	3	3	3	-1	6
	6	4	4	4	4	4	4	4	-0.5	
Y [mm]	7	5	5	5	5	5	5	5	0	
		6	6	6	6	6	6	6	0.5	
		7	8	8	8	8	8	7	1	
		8	10	10	10	10	10	8	1.5	
		9	11	12	12	12	11	9	2	
			12	13	13	13	12		2.5	
			13	14	14	14	13		3	
									3.5	
									4	
									4.5	
									5	
									5.5	
									6	
									6.5	

Table 5.7: Test Matrix for S=0.1 at X=0.5D

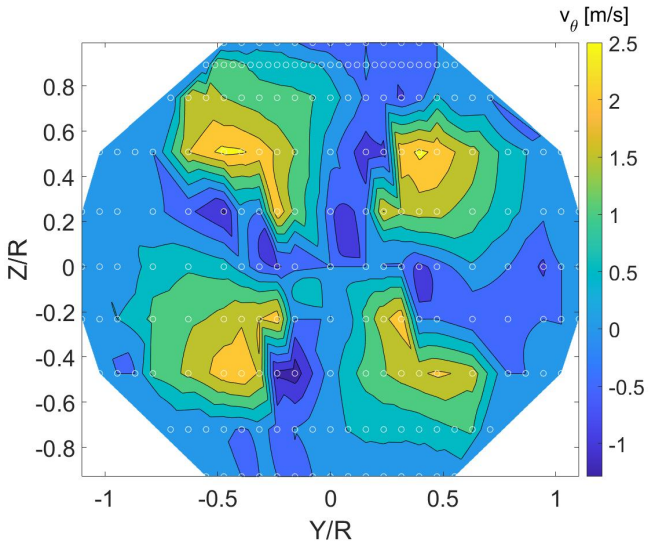

Figure 5.21: Mean interpolated V_θ field for S=0.1 at X=0.5 D.

Due to the proximity of the nozzle exit in Figure 5.21 are evident the four swirling exit region of the multichannel inset, as well as the presence of the cross strip section. While for Figures from 5.18a to 5.20 also less density velocity fields are obtained and indeed a coarser interpolation. Furthermore, in Figure 5.19 the flow fields captured appeared to lack the fourth lobe of swirling motion.

Chapter 6

Active swirl measurements

After the electrical and mechanical characterization of DBD-PAs in quiescent air and gained confidence with the pneumatic setup through the passive swirl experimental campaign, a proof of concept of the plasma-based swirling insert was mounted and tested in the jet facility. A 3D-printed short pipe insert with four stream-wise oriented DBD-PAs was mounted at the nozzle exit. Referring to the same nomenclature used in Table 4.1 the geometry values designed are presented in Table 6.1

	$t_{diel} = 1.25mm$
w_{in} $[mm]$	2
w_{ext} $[mm]$	5
L_{in} $[mm]$	57
L_{ext} $[mm]$	57
L_{plasma} $[mm]$	45

Table 6.1: Sizes of the electrodes and plasma length of the plasma-based swirling device.

Considering the acquisition time needed for the pneumatic samplings, imposed by the dynamic range of the experimental setup, it was chosen to sample, for each position, both the unforced (PA turned off) and forced jet case in order to identify also the difference between the two conditions, indeed the effect of the body forces generated by the PAs. Therefore the PAs were switched on and off during the acquisition time and weren't operating continuously. This choice was made also due to a lack of durability characterization that the writer recommends considering in further studies, once the configuration of the insert is chosen and the effect proven. For the same reason, also supported by rough observations during the electrical campaign the thinner dielectric barrier case (i.e. $t_{diel} = 1\ mm$) was discarded and

only the $t_{diel} = 1.25\ mm$ case was tested.

6.1 Experimental set up.

The experimental setup used during this activity is the same of Chapter 5.3 for the pneumatic measurement, hence the DSA module (Figure 5.11a) with his power supply, the five axial probe with the three carriages and the jet facility coupled with: the transformer cascade and the converter bridge of the high voltage - high frequency system (Figure 4.6), the power supply and the function generator object of the Chapter 4.1.1 while as oscilloscope was used an analog one: Tektronix TDS 210 (Figure 6.1)

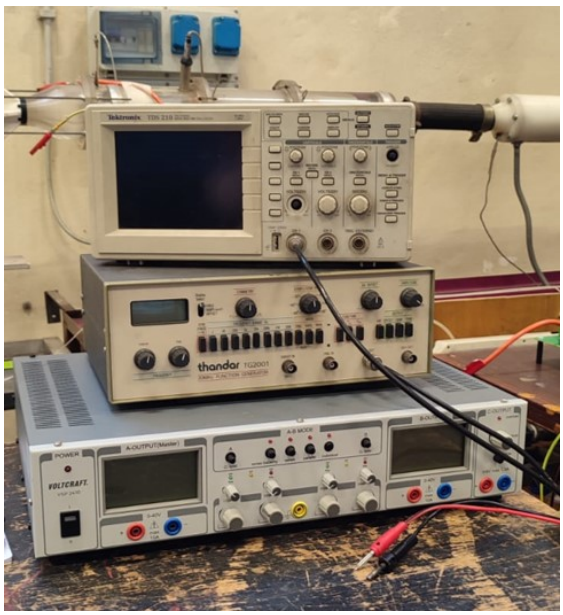

Figure 6.1: From top to bottom: oscilloscope, function generator, and power supply.

An image of the four DBD-PAs operating in absence of the axial jet stream is given in Figure 6.2.

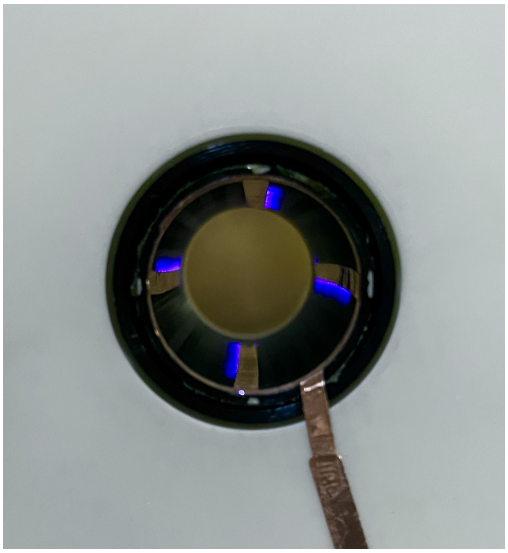

Figure 6.2: Image of the four plasma zones generated in the active swirling insert designed.

6.2 Results

Unfortunately, as said at the beginning of this chapter, the acquisition time requested by the pneumatic techniques available and the poor durability of the DBD-PAs tested in this study were relevant constraints and therefore also the higher operating voltage $V_{pp} = 12\ kV$ couldn't be taken into consideration. The sampling parameters are the same as the previous passive measurements:

- Sampling frequency: $f_s = 20\ Hz$
- Sampling period: $T_s = 45s$

while the test matrix that will follow as to be considered for each case valid for both the unforced and the forced jet case. The writer intends to underline how the sampling positions don't describe an equally spaced grid along the Y direction but were chosen in order to better capture the actuators' effect, hence the sampling grid is finer in the outer region rather than in the inner one. Also, due to the poor sensibility of the manual lab jack which confers the Z displacement and to not further increase the acquisition time, the displacement along Z was chosen constant and coarser with respect to the Y direction. Due to all these reasons the choices of the sampled points were based on the pressure values read ongoing and on the experience of previous measurements.
As first test was sampled the YZ plane at X=0.5D with the same differential reference pressure $p_6 = 66\ Pa$, as the passive case illustrated in Figure 5.21, for

the $V_{pp} = 11\ kV$ and $f_{act} = 11\ kHz$ operating conditions. The test matrix of the sampled points is reported in Table 6.2. The resulting mean interpolated velocity

Z	12.6	11.35	9.5	6.45	3.1	0	-2.95	-6	-9.15	-11.8
Y	0	0	0	0	0	0	0	0	0	0
	± 1	± 1	± 4	± 4	± 5	± 6	± 5	± 4	± 4	± 1
	± 2	± 2	± 6	± 9	± 10	± 11	± 10	± 9	± 6	± 2
	±v 2.5	± 2.5	± 7	± 10	± 11	± 11.5	± 11	± 10	± 7	± 2.5
	± 3	± 3	± 8	± 10.5	± 11.5	± 11.75	± 11.5	± 10.5	± 8	± 3
	±3.5	± 3.5	± 8.5	± 11	± 12	± 12	± 12	± 11	± 8.5	3.5
	± 5	± 4	± 9	± 11.5	± 12.5	± 12.5	± 12.5	± 11.5	± 9	4
	± 5.5	± 4.5	± 9.5	± 12	± 13	± 13	± 13	± 12	± 9.5	4.5
	± 6	± 5	± 10	± 12.5	± 13.5	± 13.5	± 13.5	± 12.5	± 10	± 5
		± 5.5	± 10.5	± 13				± 13	± 10.5	± 5.5
		± 6								6
		± 6.5								
		± 7								

Table 6.2: Test Matrix [mm] for the unforced and forced ($V_{pp} = 11\ kV$ and $f_{act} = 11\ kHz$) case at X=0.5D.

field expressed in a polar system for the unforced and forced case are reported in figure 6.3

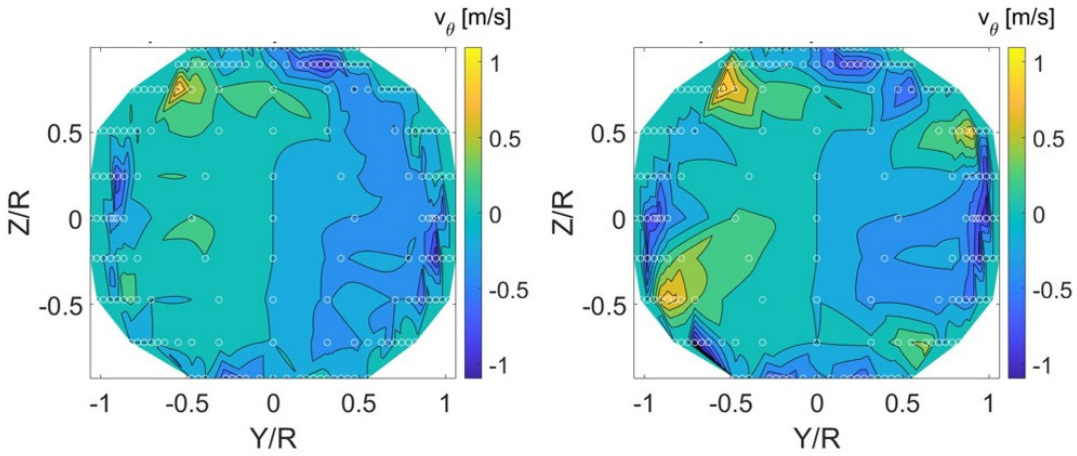

Figure 6.3: V_θ mean interpolated velocity fields for the unforced (left) and forced jet (right) ($V_{pp} = 11\ kV$, $f_{act} = 11\ kHz$) at X=0.5D, $p_6 = 66Pa$

Subtracting the mean field of the unforced jet (i.e. circular free jet) from the

forced one is possible to better highlight the effect of the actuator in the azimuthal direction. From this field (Figure 6.4) can be noted four small regions affected by the presence of the plasma actuators. In addition is quite easy to understand how due to the configuration tested and the operating conditions chosen, the control authority of the DBD-PAs for swirling purposes is poor and how they aren't able to change significantly the jet flow's behaviour. So, in conclusion, the momentum transfer caused by the plasma zones is too low with respect to the axial velocity that in the unforced case (potential core) is about $u \sim 11\ ms^{-1}$.

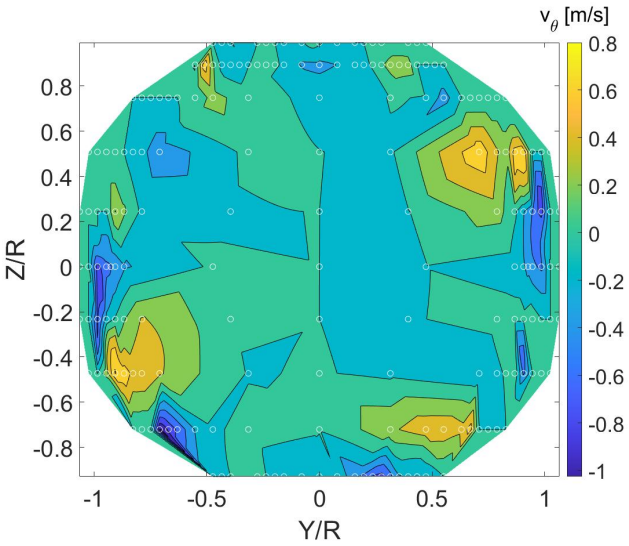

Figure 6.4: V_θ mean interpolated forced case ($V_{pp} = 11\ kV$, $f_{act} = 11\ kHz$) subtracted by the unforced one at X=0.5D, $p_6 = 66Pa$

Another YZ plane (Table 6.3) was characterized at a greater distance from the exit nozzle (X=1D) for the same electrical operating conditions ($V_{pp} = 11\ kV$ anf $f_{act} = 11\ kHz$) for a differential reference pressure of $p_6 = 96Pa$.

Z	9.5	6.45	3.1	0	-2.95	-6	-9.15
	0	0	0	0	0	0	0
Y	± 4	± 5	± 5	± 5	± 5	± 5	± 4
	± 6	± 10	± 10	± 10	± 10	± 10	± 6
	± 7	± 10.5	± 11	± 11	± 11	± 10.5	± 7
	± 8	± 11	± 12	± 12	± 12	± 11	± 8
	± 9	± 11.5	± 13	± 13	± 13	± 11.5	± 9
	± 10	± 12	± 14	± 14	± 14	± 12	± 10
	± 11	± 13	± 15	± 15	± 15	± 13	± 11
	± 13	± 14	± 16	± 16	± 16	± 14	± 13

Table 6.3: Test Matrix [mm] for the unforced and forced ($V_{pp} = 11\ kV$ and $f_{act} = 11\ kHz$) case at X=1D.

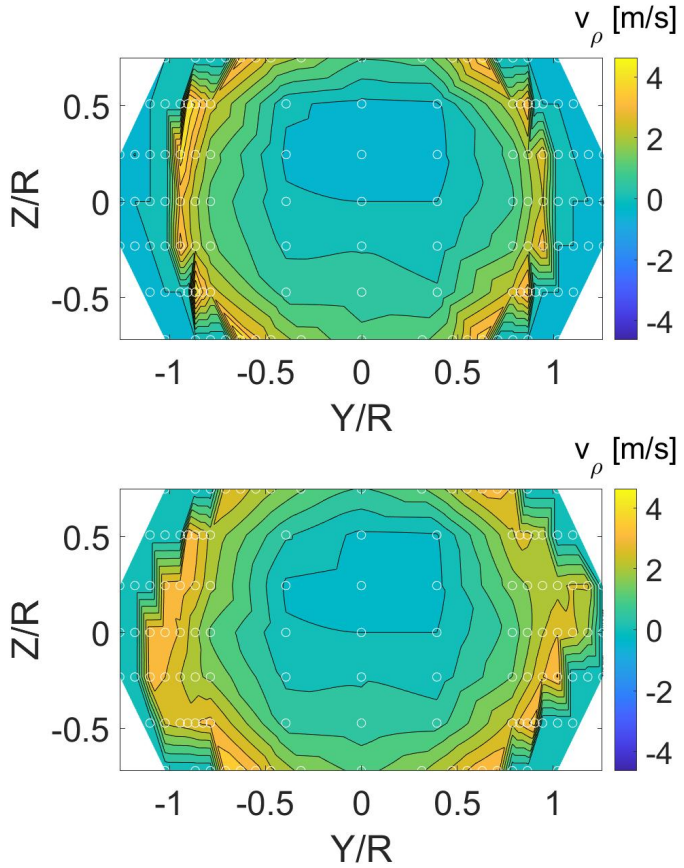

Figure 6.5: V_ρ mean interpolated velocity fields for the unforced (top) and forced (bottom) jet ($V_{pp} = 11\ kV$, $f_{act} = 11\ kHz$) at X=1D, $p_6 = 96Pa$

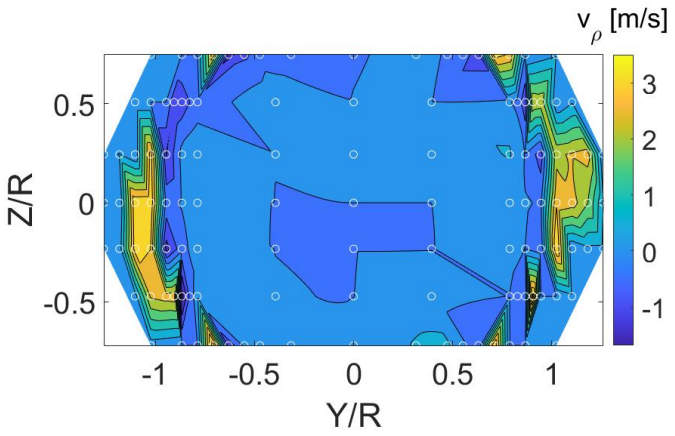

Figure 6.6: V_ρ mean interpolated field: forced case ($V_{pp} = 11\ kV$, $f_{act} = 11\ kHz$) subtracted by the unforced one at X=1D, $p_6 = 96Pa$

Looking at the radial velocity fields (Figure 6.5-6.6) is possible to notice a sort of spreading effect probably due to the light swirling effect forced by the PAs. In fact, it is well known that swirling jets, due to the presence of a centrifugal pressure gradient, spread wider than the circular ones in free stream conditions.

Chapter 7

Conclusions and outlooks

As declared in Chapter 1 this work aimed to be a preliminary investigation of the feasibility of plasma actuators as active swirling devices. The activity shown in this work doesn't allow us to declare if plasma-based swirling could be the best active swirling generator but could be seen as the preliminary step for future studies in the department laboratory "Modesto Panetti" of the Polytechnic University of Turin. Starting from a facility previously intended only for educational purposes, and only with the instrumental already available in the laboratory, the activity carried out path the way for a new research topic. The results obtained with this preliminary design show signs of a broadening effect due to the forcing of plasma actuators nevertheless, only a localized induced swirling behavior is seen. These statements have to be taken as not universal because of the limited test cases and since they are limited to the experimental conditions under consideration during the activities. In particular, significant optimizations should be implemented: the dielectric material must be changed in order to obtain a better momentum injection and for durability issues. This last point was a challenging constraint also for the measurement techniques available during these months in the department laboratory. Other measurement techniques should be taken into consideration: field measurements like Stereo PIV or IR thermography in the case of impinging configuration over a heated thin surface would be optimal candidates; point techniques, like the one used in this work, are also valuable but they will never reach the vectors density of a field obtained through Stereo PIV. Furthermore, the effort spent by the user doesn't pay the poor accuracy of the obtained results or fluid dynamics aspects that could be explored. Point techniques like hot wire anemometry (HWA), for instance using an X-probe, could allow the user to investigate turbulent fluctuations due to a greater time resolution but this choice may present also challenging aspects like the calibration of the probe and compatibility with the plasma zone and their electromagnetic effects that could or not affect the measurements. What is certain is that for future studies at least the dynamic range of the current experimental

setup has to be increased. The experimental campaigns carried out in chapters 4.1-4 could be used as a reference for future designs remaining aware that the results obtained here don't present optimizations at electrical consumption level as highlighted by the efficiency outputs due also by poor mechanical effects and indeed control authority.

Bibliography

[1] Ashwani K Gupta, David G Lilley, and Nick Syred. «Swirl flows». In: *Tunbridge Wells* (1984) (cit. on pp. 4, 6, 59).

[2] Gerardo Paolillo, Carlo Salvatore Greco, Tommaso Astarita, and Gennaro Cardone. «Effects of the swirl number, Reynolds number and nozzle-to-plate distance on impingement heat transfer from swirling jets». In: *International Journal of Heat and Mass Transfer* 197 (2022), p. 123284 (cit. on pp. 5, 6).

[3] Mattia Contino, Gerardo Paolillo, Carlo Salvatore Greco, Tommaso Astarita, and Gennaro Cardone. «Simultaneous visualization of the velocity and wall temperature fields in impinging swirling jets». In: *Optics and Lasers in Engineering* 158 (2022), p. 107165 (cit. on p. 5).

[4] Andrea Ianiro and Gennaro Cardone. «Heat transfer rate and uniformity in multichannel swirling impinging jets». In: *Applied Thermal Engineering* 49 (2012), pp. 89–98 (cit. on pp. 5, 7, 8, 45, 59).

[5] Sergey V Alekseenko, Artur V Bilsky, Vladimir M Dulin, and Dmitriy M Markovich. «Experimental study of an impinging jet with different swirl rates». In: *International Journal of Heat and Fluid Flow* 28.6 (2007), pp. 1340–1359 (cit. on pp. 6, 10, 11).

[6] Nicholas Syred. «A review of oscillation mechanisms and the role of the precessing vortex core (PVC) in swirl combustion systems». In: *Progress in Energy and Combustion Science* 32.2 (2006), pp. 93–161 (cit. on p. 6).

[7] N Syred and JM Beer. «Combustion in swirling flows: a review». In: *Combustion and flame* 23.2 (1974), pp. 143–201 (cit. on p. 7).

[8] Gang Li, Xi Jiang, Yujun Zhao, Cunxi Liu, Qi Chen, Gang Xu, and Fuqiang Liu. «Jet flow and premixed jet flame control by plasma swirler». In: *Physics Letters A* 381.13 (2017), pp. 1158–1162 (cit. on p. 7).

[9] L Huang and MS El-Genk. «Heat transfer and flow visualization experiments of swirling, multi-channel, and conventional impinging jets». In: *International Journal of Heat and Mass Transfer* 41.3 (1998), pp. 583–600 (cit. on pp. 8, 9).

[10] CF Gallo. «Coronas and gas discharges in electrophotography: A review». In: *IEEE Transactions on Industry Applications* 6 (1975), pp. 739–748 (cit. on p. 13).

[11] Jochen Kriegseis, Bernhard Simon, and Sven Grundmann. «Towards in-flight applications? A review on dielectric barrier discharge-based boundary-layer control». In: *Applied Mechanics Reviews* 68.2 (2016), p. 020802 (cit. on p. 13).

[12] Mo Samimy, Nathan Webb, and Ata Esfahani. «Reinventing the wheel: excitation of flow instabilities for active flow control using plasma actuators». In: *Journal of Physics D: Applied Physics* 52.35 (2019), p. 354002 (cit. on p. 14).

[13] M Kearney-Fischer, J-H Kim, and M Samimy. «Control of a high Reynolds number Mach 0.9 heated jet using plasma actuators». In: *Physics of Fluids* 21.9 (2009) (cit. on p. 14).

[14] Thomas C Corke, C Lon Enloe, and Stephen P Wilkinson. «Dielectric barrier discharge plasma actuators for flow control». In: *Annual review of fluid mechanics* 42 (2010), pp. 505–529 (cit. on p. 15).

[15] Christopher L Kelley, Patrick O Bowles, John Cooney, Chuan He, Thomas C Corke, Bradley A Osborne, Joseph S Silkey, and Joseph Zehnle. «Leading-edge separation control using alternating-current and nanosecond-pulse plasma actuators». In: *AIAA journal* 52.9 (2014), pp. 1871–1884 (cit. on p. 15).

[16] N Benard, P Braud, G Touchard, and E Moreau. «Detachment and attachment of an axisymmetric non-reactive jet with turbulent shear layer: control by plasma actuator». In: *Experimental thermal and fluid science* 32.6 (2008), pp. 1193–1203 (cit. on p. 15).

[17] YE Akansu, F Karakaya, and A Şanlısoy. «Active control of flow around NACA 0015 airfoil by using DBD plasma actuator». In: *EPJ web of conferences*. Vol. 45. EDP Sciences. 2013, p. 01008 (cit. on p. 16).

[18] Sven Grundmann and Cameron Tropea. «Experimental damping of boundary-layer oscillations using DBD plasma actuators». In: *International Journal of Heat and Fluid Flow* 30.3 (2009), pp. 394–402 (cit. on pp. 16, 17, 21).

[19] Jin-Hwa Kim and Mo Samimy. «Effects of active control on the flow structure in a high Reynolds number supersonic jet». In: *International Journal of Flow Control* (2009) (cit. on pp. 17, 18).

[20] Michael Crawley, Martin Kearney-Fischer, and Mo Samimy. «Control of a supersonic rectangular jet using plasma actuators». In: *18th AIAA/CEAS Aeroacoustics Conference (33rd AIAA Aeroacoustics Conference)*. 2012, p. 2211 (cit. on pp. 18, 19).

[21] Jochen Kriegseis, Benjamin Möller, Sven Grundmann, and Cameron Tropea. «Capacitance and power consumption quantification of dielectric barrier discharge (DBD) plasma actuators». In: *Journal of Electrostatics* 69.4 (2011), pp. 302–312 (cit. on pp. 22, 23).

[22] Abraham Savitzky and Marcel JE Golay. «Smoothing and differentiation of data by simplified least squares procedures.» In: *Analytical chemistry* 36.8 (1964), pp. 1627–1639 (cit. on p. 24).

[23] Jerry Westerweel and Fulvio Scarano. «Universal outlier detection for PIV data». In: *Experiments in fluids* 39 (2005), pp. 1096–1100 (cit. on p. 37).